

1
2
3
4
5
6
7
8
9
10
11

Scalable statistics of correlated random variables and extremes applied
to deep borehole porosities

A. Guadagnini^{1,2}, S. P. Neuman¹, T. Nan¹, M. Riva^{1,2} and C. L. Winter¹

1. Department of Hydrology and Water Resources, University of Arizona, Tucson, Arizona
85721, USA

2. Dipartimento di Ingegneria Civile e Ambientale, Politecnico di Milano, Piazza L. Da Vinci 32,
20133 Milano, Italy

ABSTRACT

12
13 We analyze scale-dependent statistics of correlated random hydrogeological variables
14 and their extremes using neutron porosity data from six deep boreholes, in three diverse
15 depositional environments, as example. We show that key statistics of porosity increments
16 behave and scale in manners typical of many earth and environmental (as well as other)
17 variables. These scaling behaviors include a tendency of increments to have symmetric, non-
18 Gaussian frequency distributions characterized by heavy tails that decay with separation distance
19 or lag; power-law scaling of sample structure functions (statistical moments of absolute
20 increments) in midranges of lags; linear relationships between log structure functions of
21 successive orders at all lags, known as extended self-similarity or ESS; and nonlinear scaling of
22 structure function power-law exponents with function order, a phenomenon commonly attributed
23 in the literature to multifractals. Elsewhere we proposed, explored and demonstrated a new
24 method of geostatistical inference that captures all of these phenomena within a unified
25 theoretical framework. The framework views data as samples from random fields constituting
26 scale-mixtures of truncated (monofractal) fractional Brownian motion (tfBm) of fractional
27 Gaussian noise (tfGn). Important questions not addressed in previous studies concern the
28 distribution and statistical scaling of extreme incremental values. Of special interest in hydrology
29 (and many other areas) are statistics of absolute increments exceeding given thresholds, known
30 as peaks over threshold or POTs. In this paper we explore the statistical scaling of data and, for
31 the first time, corresponding POTs associated with samples from scale-mixtures of tfBm or tfGn.
32 We demonstrate that porosity data we analyze possess properties of such samples and thus
33 follow the theory we proposed. The porosity data are of additional value in revealing a
34 remarkable cross-over from one scaling regime to another at certain lags. The phenomena we

- 35 uncover are of key importance for the analysis of fluid flow and solute as well as particulate
- 36 transport in complex hydrogeologic environments.

1. INTRODUCTION

37

38

39

40

41

42

43

44

45

46

47

48

49

50

51

52

53

54

Hydrogeologic variables such as log permeability are known to vary with scales of measurement, observation, domain of investigation, spatial correlation and resolution (Neuman and Di Federico, 2003). The statistics of these and diverse environmental (as well as earth, financial, astrophysical, biological and many other) variables are likewise known to vary with scale. This is especially true of statistics characterizing spatial and/or temporal increments of these variables. Symptoms of such statistical scaling include irregular spatial variability, persistence or antipersistence of increments (large and small values tending to either persist or alternate rapidly in space and/or time); tendency of increments to have symmetric, non-Gaussian frequency distributions characterized by heavy tails that often decay with separation distance or lag; power-law scaling of sample structure functions (statistical moments of absolute increments) in midranges of lags, with breakdown in power-law scaling at small and/or large lags; linear relationships between log structure functions of successive orders at all lags, also known as extended self-similarity or ESS; and nonlinear scaling of structure function power-law exponents with function order. The traditional interpretation of these widely-documented behaviors has been based on the concept of multifractals. This, however, does not explain observed breakdown in power-law scaling at small and large lags or extended power-law scaling (Neuman et al., 2013 and references therein).

55

56

57

58

59

Of special concern are the statistics of extremes, which have received much attention among hydrologists (Katz et al., 2002) and others concerned with a wide range of phenomena including snow avalanches on mountain slopes (Ancey, 2012); rupture events associated with the propagation of cracks or sliding along faults in brittle materials including rock failure, landslides and earthquakes (Amitrano, 2012; Lei, 2012; Main and Naylor, 2012) as well as volcanic

60 eruptions, landslides, wildfires and floods (Sachs et al., 2012; Schoenberg and Patel, 2012;
61 Süveges and Davison, 2012); demographic and financial crises (Akaev et al., 2012; Janczura and
62 Weron, 2012); neuronal avalanches and coherence potentials in the mammalian cerebral cortex
63 (de Arcangelis, 2012; Plenz, 2012); citations of scientific papers (Golosovsky and Solomon,
64 2012); and distributions of city sizes (Pisarenko and Sornette, 2012). Extreme values cluster
65 around heavy tails of data frequency distributions which are often modeled as stretched
66 exponential, lognormal or power functions. There is growing evidence that these frequency
67 distributions, as well as other geospatial and/or temporal statistics of many data, vary with scale.
68 A key related question concerns the scale dependence of frequency distributions (typically
69 generalized extreme value or GEV in the case of block extrema and generalized Pareto
70 distribution or GPD in the case of peaks over thresholds or POTs, e.g. Embrechts et al., 1997)
71 and statistics of extremes at the tails of the original data distributions (e.g. Riva et al., 2013a).

72 In this paper we explore the statistical scaling of variables and, for the first time,
73 corresponding POTs using as an example neutron porosity data and their POTs from six deep
74 boreholes in three different depositional environments. These data are of interest because, as we
75 show below, (a) they possess statistics that scale in manners typical of many earth,
76 environmental and other variables and (b) reveal a remarkable cross-over from one scaling
77 regime to another at certain separation distances or lags. The phenomena we uncover vis-à-vis
78 neutron porosity data, and corresponding extremes, are of critical importance for the analysis of
79 fluid flow and solute as well as particulate transport in complex hydrogeologic environments.
80 This is so because spatial variability of porosity controls fluid flow velocity distributions in
81 geologic media and has an impact on solute and particulate concentration dynamics. Extreme
82 values of porosity are particularly relevant to depositional processes responsible for the

83 development of preferential flow paths through heterogeneous porous and fractured media.
84 Neutron porosity logs are widely used to characterize stratigraphic sequences and the
85 geostatistical description of geological structures of lithotypes in multilayer systems of aquifers
86 and aquitards (e.g., Barrash and Reboulet, 2004, Tronicke and Holliger, 2005). Combined with
87 laboratory-determined particle size distributions, porosity data may allow one to infer spatial
88 distributions (see review of Vuković and Soro, 1992) and covariances (Riva et al., 2014) of
89 hydraulic conductivity.

90 Statistical scaling of hydrogeological data such as permeability or hydraulic conductivity
91 has been studied amongst others by Painter (2001), Meerschaert et al. (2004), Kozubowski et al.
92 (2006), Siena et al. (2012, 2014), Riva et al. (2013b, 2013c), and Guadagnini et al. (2012, 2013,
93 2014). Whereas research in the subsurface hydrology literature has not addressed specifically the
94 distribution and statistical scaling of extreme incremental values, spatial correlations between
95 values significantly in excess of the mean have been studied vis-à-vis variables such as
96 transmissivity and their relevance to transport processes has been highlighted. Sanchez-Vila et al.
97 (1996) conjectured that observed scale dependence of transmissivities estimated from large scale
98 pumping tests could be related to strong connectivity between regions of elevated transmissivity,
99 as opposed to spatial persistence of average or low transmissivity values. Spatial correlation of
100 extreme conductivity values was examined for the first time by Gómez-Hernández and Wen
101 (1998). In these authors' opinion the standard multi-Gaussian assumption was not consistent
102 with observed short solute travel times resulting from fast spatially connected pathways.
103 Connectivity of high permeability zones thus became an important concept underlying some
104 modern interpretations of effective conductivity and solute travel time (see for example Meier et
105 al., 1998; Wen and Gómez-Hernández, 1998; Western et al., 2001; Fogg et al., 2000; Zinn and

106 Harvey, 2003; Knudby and Carrera, 2005, 2006; Knudby et al., 2006; Nield, 2008, and
107 references therein). The above ideas have motivated the development of multi-point
108 geostatistical methods of analysis such as those described in a recent special issue of the journal
109 *Mathematical Geosciences* on 20 years of multi-point statistics (e.g., Renard and Mariethoz
110 (2014) and Mariethoz and Renard (2014) and references therein).

111 Notably, attempts by hydrologists to investigate the manner in which statistics of
112 extremes vary with scale have centered almost exclusively on peak rainfall intensities and stream
113 flows. Whereas some have found statistical measures of rainfall extremes to exhibit linear
114 (sometimes termed simple) scaling (Menabde et al., 1999; Garcia-Bartual and Schneider, 2001;
115 De Michele et al., 2001) under at least some conditions (Burlando and Rosso, 1996; Veneziano
116 and Furcolo, 2002; Yu et al., 2004), most authors describe them by means of nonlinear (often
117 called multiscaling) models (Burlando and Rosso, 1996; Veneziano and Furcolo, 2002; Castro et
118 al., 2004; Langousis and Veneziano, 2007; Mohymont and Demarée, 2006). Statistical measures
119 of peak stream flows were considered by Javelle et al. (1999), Menabde and Sivapalan (2001)
120 and Rigon et al. (2011) to scale linearly. Work on the scaling of GEVs and/or GPDs associated
121 with extreme rainfall and/or stream flow was reported amongst others by Nguyen et al. (1998),
122 Menabde et al. (1999), Menabde and Sivapalan (2001), Willems (2000), Trefry et al. (2005),
123 Veneziano et al. (2009) and Veneziano and Yoon (2013). The general tendency has been to
124 interpret linear scaling as a manifestation of monofractal behavior analogous to that of fractional
125 Brownian motion (fBm) or fractional Gaussian noise (fGn). Nonlinear scaling has commonly
126 been attributed to multifractal behavior, a viewpoint espoused originally by Schertzer and
127 Lovejoy (1987) and expanded on recently by Veneziano and Yoon (2013).

128 Work by our group has demonstrated theoretically (Neuman 2010, 2011; Guadagnini and
129 Neuman, 2011; Siena et al., 2012; Neuman et al., 2013), computationally (Guadagnini et al.,
130 2012; Neuman et al., 2013) and on the basis of varied pedological, hydrological and
131 hydrogeological data (Siena et al., 2012, 2014; Riva et al., 2013b, 2013c; Guadagnini et al.,
132 2012, 2013, 2014) that statistical scaling behaviors of the kind traditionally attributed to
133 multifractals can be interpreted more simply and consistently by viewing the data as samples
134 from stationary sub-Gaussian random fields subordinated to truncated fBm (tfBm) or fGn (tfGn).
135 Such sub-Gaussian fields are scale mixtures of stationary Gaussian fields with random variances
136 (Andrews and Mallows, 1974; West, 1987) that we model as being log-normal or Lévy stable
137 (Samorodnitsky and Taqqu, 1994). In this sense our approach bears partial relationship to
138 cascades of Gaussian-scale mixtures that Ebtehaj and Foufoula-Georgiou (2011) use to
139 reproduce coherent structures and extremes of precipitation reflectivity images in the wavelet
140 domain.

141 Our analysis suggests that, quantitatively, the statistics of neutron porosity increments
142 and their POTs at intra-layer vertical separation scales (or lags) differ from those at inter-layer
143 scales. Qualitatively, however, the statistics of porosity increments at each of these two scales
144 behave in a manner that the literature would typically associate with multifractals. This behavior
145 includes all statistical scaling symptoms described above. Our alternative interpretation of the
146 data allows us to obtain maximum likelihood (ML) estimates of all parameters characterizing the
147 underlying truncated sub-Gaussian fields at both intra- and inter-layer scales. Most importantly,
148 we offer what appears to be the first data-driven exploration (following a synthetic study of
149 outliers by Riva et al., 2013a) of how statistics of POTs associated with such families of sub-
150 Gaussian fields vary with scale.

151
152
153
154
155
156
157
158
159
160
161
162
163
164
165
166
167
168
169
170
171
172

2. SOURCE OF NEUTRON POROSITY DATA

As stated in Section 1, we illustrate and explore our approach on neutron porosity data from six deep vertical boreholes in three different depositional environments. These are part of a broader set of geophysical logs from the same boreholes, previously described and analyzed within a multifractal framework by Dashtian et al. (2011), provided to us courtesy of Professor Muhammad Sahimi, University of Southern California. Three of the wells (numbered here 1, 2 and 3) are drilled in the Maroon field within which gas drive is used to produce oil and natural gas, wells 4 and 5 in the Ahwaz oil field, and well 6 in the Tabnak gas field. The Maroon and Ahwaz fields in southwestern Iran, and the Tabnak field in southern Iran, have distinct geologies. Whereas carbonate rock content is highest in the Tabnak and lowest in the Maroon and Ahwaz fields, the opposite is true about sandstone content. Though we do not have information about the relative geographic locations of the six wells, we note that Dashtian et al. (2011) analyzed data from each well independently of those from the remaining five wells. We do the same on the assumption that distances between the wells are sufficiently large to allow treating data from each well as being statistically independent of the rest.

3. THEORETICAL BASIS AND METHOD OF INFERENCE

Summary information about the available neutron porosity (P) data is listed in Table 1. As the sampling interval between available values in Well 6 is half of that in Wells 1 - 5, we disregard every other measurement in analyzing these data, leaving a total of 4,267 values. Most of our analysis concerns increments in recorded P values at various separation distances or lags, s , in each well. Lags are taken to be integer multiples, $s = s_n \times \Delta z$, of the vertical spacing, $\Delta z = 0.1524$ m, between recorded values.

173 As stated in Section 1, we view the data as samples from stationary sub-Gaussian random
 174 fields subordinated to truncated fBm (tfBm) or fGn (tfGn). Sub-Gaussian random variables,
 175 defined in Appendix A following standard statistical terminology (e.g., Samorodnitsky and
 176 Taqqu, 1994), are scale mixtures of Gaussian variables with random variances. We consider two
 177 sub-Gaussian variables, one α -stable with Gaussian variances that are $\alpha/2$ -stable, and another
 178 normal-lognormal (NLN) variable with lognormal Gaussian variances. There is no physical basis
 179 for their choice, just as there usually is no such basis for working with the Gaussian distribution.
 180 Lévy- (or α -) stable probability distributions are frequently employed due to their ability to
 181 interpret heavy tails displayed by empirical distributions of data. While convenient in this sense,
 182 this model has the drawback of being associated with densities with diverging moments of order
 183 larger than α , notably the variance (e.g., Neuman et al., 2013 and references therein). The use of
 184 a lognormal subordinator provides us with the ability to represent tailing behaviors reasonably
 185 well with the additional benefit that associated densities possess finite moments of all orders.
 186 Regardless of this choice, our approach is compatible with diverse types of subordinators. Using
 187 maximum likelihood (ML) we compare the ability of the above two subordinators to (a) capture
 188 critical distributional features of our data and (b) and yield reliable parameters of the underlying
 189 sub-Gaussian random fields.

190 Statistical scaling of the data is analyzed in part on the basis of sample structure
 191 functions, $S_N^q(s_n)$, of order q . Structure functions are moments of order q of absolute increments
 192 (e.g. Frisch, 1995). The corresponding sample moments are constructed with $N(s_n)$ absolute
 193 increments at normalized (by Δz) lags s_n ,

$$194 S_N^q(s_n) = \frac{1}{N(s_n)} \sum_{j=1}^{N(s_n)} |\Delta P_j(s_n)|^q \tag{1}$$

195 where $\Delta P_j(s_n)$ is the j -th increment of P values separated by lag s_n . The variable P is said
 196 exhibits power-law scaling if $S_N^q(s_n) \propto s_n^{\xi(q)}$ where the power or scaling exponent, $\xi(q)$,
 197 depends solely on the order q . The exponent is estimated through linear fits of $\log(S_N^q)$ to $\log(s_n$
 198) within the range of lags where such linear behavior is indicated. We refer to this approach of
 199 assessing and quantifying power-law scaling as method of moments.

200 As shown by Neuman et al. (2013 and references therein), another way to assess the
 201 dependence of scaling exponents $\xi(q)$ on q is through extended self-similarity (ESS) or extended
 202 power-law scaling. ESS is an empirical approach originally introduced by Benzi et al. (1993a,
 203 1993b, 1996) to widen the range of lags over which velocities in fully developed turbulence scale
 204 according to Equation (1). The approach calls for plotting the S_N^{q+1} versus S_N^q for various q
 205 values and quantifying the resulting linear dependence between them (see Neuman et al., 2013
 206 and references therein). In this work we apply both methods to available neutron porosity data.

207 To estimate parameters characterizing the distribution of the underlying (Gaussian) tfBm
 208 or tfGn, we consider the zero-mean tfBm $G'(x; \lambda_l, \lambda_u)$ defined by Di Federico and Neuman
 209 (1997) as a Gaussian random function of space having variance

$$210 \quad \sigma_G^2(\lambda_l, \lambda_u) = \sigma_G^2(\lambda_u) - \sigma_G^2(\lambda_l), \quad (2)$$

211 variogram or semi-structure function of second order

$$212 \quad \gamma_G(s; \lambda_l, \lambda_u) = \gamma_G(s; \lambda_u) - \gamma_G(s; \lambda_l), \quad (3)$$

213 and integral autocorrelation scale

$$214 \quad I(\lambda_l, \lambda_u) = \frac{2H}{1+2H} \frac{\lambda_u^{1+2H} - \lambda_l^{1+2H}}{\lambda_u^{2H} - \lambda_l^{2H}} \quad (4)$$

215 where, for $m = l, u$,

216 $\sigma_G^2(\lambda_m) = A\lambda_m^{2H} / 2H,$ (5)

217 $\gamma_G(s; \lambda_m) = \sigma_G^2(\lambda_m) \rho(s / \lambda_m),$ (6)

218 A is a coefficient, H is a Hurst scaling exponent and s is lag. The tfBm variogram $\gamma_G(s; \lambda_l, \lambda_u)$ is
 219 a weighted integral of variograms characterizing stationary Gaussian fields, or modes, having
 220 integral scales λ and variances $\sigma^2(\lambda) = A\lambda^{2H} / 2H$, between lower and upper cutoff scales, λ_l
 221 and λ_u , respectively. Here we consider modes having Gaussian variograms in which case

222
$$\rho(s / \lambda_m) = \left[1 - \exp\left(-\frac{\pi s^2}{4 \lambda_m^2}\right) + \left(\frac{\pi s^2}{4 \lambda_m^2}\right)^H \Gamma\left(1-H, \frac{\pi s^2}{4 \lambda_m^2}\right) \right] \quad 0 < H < 1$$
 (7)

223 where $\Gamma(\cdot, \cdot)$ is the incomplete gamma function. In the limits $\lambda_l \rightarrow 0$ and $\lambda_u \rightarrow \infty$, $\gamma_G(s; \lambda_l, \lambda_u)$
 224 tends to a power variogram (PV) $\gamma^2(s) = Bs^{2H}$ where $B = A(\pi/4)^{2H/2} \Gamma(1-2H/2) / 2H$, Γ
 225 being the gamma function. The stationary tfBm $G'(x; \lambda_l, \lambda_u)$ thus tends to nonstationary fBm,
 226 $G'(x; 0, \infty)$, the stationary increments of which, $\Delta G(x, x+s; 0, \infty)$, form fGn. It follows that
 227 when $\lambda_u < \infty$, $\gamma_G(s; \lambda_l, \lambda_u)$ is a truncated power variogram (TPV) characterizing a (stationary)
 228 truncated version of fBm (tfBm).

229 We treat neutron porosity increments in each borehole as a sample from a zero-mean
 230 random field, $\Delta Y(x, x+s; \lambda_l, \lambda_u)$, subordinated to tfBm according to (see Appendix A)

231 $\Delta Y(x, x+s; \lambda_l, \lambda_u) = W^{1/2} \Delta G(x, x+s; \lambda_l, \lambda_u)$ (8)

232 where $s \geq 0$ is lag and the subordinator, W , is a non-negative random variable independent of
 233 ΔG (and of G'). As stated above, we allow W to be Lévy stable or log-normal. Appendix A
 234 explains that, in the first case, W is $\alpha/2$ -stable totally skewed to the right of zero (hence non-

235 negative) with scale parameter $\sigma_s = \left(\cos \frac{\pi\alpha}{4}\right)^{2/\alpha}$, unit skewness and zero shift. The
 236 corresponding univariate pdf of $\Delta Y(x, x+s; \lambda_l, \lambda_u)$ is symmetric α -stable with zero skewness
 237 and shift. The pdf possesses heavy, power-law tails. In the second case $W^{1/2} = e^V$ where V is
 238 zero-mean Gaussian with variance $\sigma_v^2 = (2-\alpha)^2$. This renders $W^{1/2} \equiv 1$ when $\alpha = 2$ and its pdf
 239 increasingly skewed to the right as α diminishes. The corresponding univariate normal-
 240 lognormal (NLN) pdf of $\Delta Y(x, x+s; \lambda_l, \lambda_u)$ possesses heavier tails than the exponential tails of
 241 the Gaussian to which NLN tends asymptotically as α increases toward 2. Whereas α -stable
 242 variables do not possess finite moments of order $\geq \alpha$, all moments of NLN variables are finite.
 243 Parameters of the variogram characterizing the underlying Gaussian field are estimated through
 244 ML model calibration, as detailed in Section 7 for the two types of subordinators we consider.

245 4. FREQUENCY DISTRIBUTIONS OF NEUTRON POROSITY DATA

246 Figure 1 shows how the neutron porosity data vary with depth in Wells 1, 4, 5 and 6.
 247 Frequency distributions of deviations, $P' = P - P_a$, from average values, P_a , in Wells 1, 4 and 6
 248 are plotted on arithmetic and semi-logarithmic scales in Figure 2. The empirical frequency
 249 distributions exhibit sharp peaks, asymmetry and slight bimodality. Also shown in Figure 2 are
 250 maximum likelihood (ML) fits of a Gaussian and two sub-Gaussian probability density functions
 251 (pdfs) to the empirical frequency distributions. Figure 1 shows that neutron porosity values in
 252 Well 6 exhibit greater variability than in other wells. This could be due to a larger carbonate
 253 content in formations penetrated by Well 6 than in those penetrated by other wells (see Section
 254 2), rendering the former more heterogeneous than the rest.

255 ML fits to Gaussian and α -stable pdfs is accomplished with a code developed by Nolan
 256 (2001) and to NLN using a code we have written in Matlab. The quality of these fits is variable;

257 in the case of Well 1, the NLN model is seen to fit the empirical frequency distribution slightly
258 better than do the other two models but, in the case of Well 6, the α -stable model is seen to be
259 best and Gaussian model worst. Formal Kolmogorov-Smirnov, χ^2 and Shapiro-Wilk tests
260 conducted on some of the data tend to reject the Gaussian model at a significance level of 0.05.

261 **5. FREQUENCY DISTRIBUTIONS OF NEUTRON POROSITY INCREMENTS**

262 Rather than presenting results in terms of lag s we report them below in terms of
263 normalized (by Δz) integer values, s_n . Figure 3 shows how increments $\Delta P(s_n)$ at three different
264 normalized lags ($s_n = 1, 32, 1024$) vary with sequential (integer) vertical position in Wells 1
265 (Maroon field), 4 (Ahwaz field) and 6 (Tabnak field).

266 Frequency distributions of $\Delta P(s_n)$ at the same three lags in Wells 1 and 4 are plotted on
267 semi-logarithmic scale in Figure 4. The empirical frequency distributions exhibit pronounced
268 symmetry with sharp peaks and heavy tails, which decay toward Gaussian shapes as lags
269 increase. At all lags, the empirical frequency distributions of increments are represented quite
270 closely by α -stable and NLN models fitted to them by ML. Negative log likelihood (NLL)
271 measures of best fit associated with these two models as well as values of the Kashyap (1982)
272 information criterion, KIC, demonstrate that they fit the empirical frequency distributions
273 equally well (not shown). The same is true for all increments in all other wells. Frequency
274 distributions of $\Delta P(s_n)$ plotted for two normalized lags in Well 6 (Figure 5) are likewise
275 symmetric with sharp peaks and heavy tails which, however, do not decay with lag. Empirical
276 frequency distributions of $\Delta P(s_n)$ in Well 6 are represented equally well by α -stable and NLN
277 models.

278 Figure 6 shows how estimates $\hat{\alpha}$ and $\hat{\sigma}$ of stability and scale parameters, respectively,
 279 characterizing α -stable distribution models (see Appendix A) of neutron porosity increments in
 280 all wells vary with normalized lag. Estimates $\hat{\alpha}$ of the stability index, α , in Wells 1 - 3
 281 (Maroon field) and 4 - 5 (Ahwaz field) exceed 1 and increase asymptotically toward 2 with
 282 increasing lag, confirming that the increments become Gaussian at large lags. In Well 6 (Tabnak
 283 field) $\hat{\alpha}$ fluctuates around a value that exceeds 1 by a small amount. Estimates $\hat{\sigma}$ of the scaling
 284 index σ , which measures the width of the α -stable distribution, first increase with lag and then
 285 stabilize in all wells. All these behaviors are consistent with sub-Gaussian random fields
 286 associated with α -stable subordinators; whether or not α does or does not grow with lag
 287 depends on how these fields are generated (see Riva et al., 2013c and Neuman et al., 2013). We
 288 do not show but note that parameters of NLN distribution models fitted to the increments also
 289 vary with lag in a way that renders them asymptotically Gaussian at large lags, with the
 290 exception of Well 6.

291 6. STATISTICAL SCALING OF NEUTRON POROSITY INCREMENTS

292 Next we analyze the scaling behavior of sample structure functions, $S_N^q(s_n)$, of order q
 293 defined in Equation (1). Figure 7 shows how such structure functions of orders $q = 0.5, 1.0$ and
 294 2.0 vary with s_n in Wells 1 (Maroon) and 6 (Tabnak). Log-log regression lines fitted to the data
 295 separately at vertical distance scales $s_n < 10$ and $s_n > 12$ suggest, at relatively high levels of
 296 confidence (coefficients of determination, R^2 , ranging from 0.98 to 0.99 at $s_n < 10$ and from
 297 0.89 to 0.99 at $s_n > 12$), that $S_N^q(s_n)$ varies as a power of s_n in each of these two scale ranges.
 298 Power-law exponents are larger at small ($s_n < 10$) than at large ($s_n > 12$) lags. We thus have a
 299 cross-over between two diverse power-law regimes at distance scales 1.5 - 1.8 m delineated in

300 Figure 7 by a dashed red line. We interpret the power-law scaling of $S_N^q(s_n)$ with s_n at $s_n < 10$
301 to represent variability within, and that at $s_n > 12$ variability between, sedimentary layers at each
302 site. Similar dual power-law scaling behavior is exhibited by structure functions of increments
303 from Wells 2 - 5 (not shown). The identification of layers of diverse geomaterials is related to
304 depositional processes which take place over time in any sedimentary basin of the kind we deal
305 with here. Dashtian et al. (2011) concluded that these formations are layered based on complete
306 suites of well logs at each of the three sites. We note further that a similar dual-scaling
307 phenomenon has recently been reported by Siena et al. (2014) vis-a-vis porosities and specific
308 surface areas imaged using x-ray computer micro-tomography throughout a millimeter-scale
309 block of Estailades limestone, at a spatial resolution of 3.3 μm , as well as Lagrangian velocities
310 computed by solving the Stokes equation in the sample pore space.

311 Following the most recent examples of Guadagnini et al. (2013, 2014) we use the method
312 of moments described in Section 3 to obtain estimates, \hat{H}_w and \hat{H}_b , of Hurst scaling exponents,
313 H_w and H_b , characterizing the within- and between-layers scaling behaviors of neutron porosity
314 increments, respectively, in each well. \hat{H}_w and \hat{H}_b are set equal to the slopes, $\zeta_w(q = 1)$ and $\zeta_b(q$
315 $= 1)$, of regression lines fitted to $S_N^1(s_n)$ on log-log scale at $s_n < 10$ and $s_n > 12$, respectively.
316 Values of these estimates are listed, for all six wells, in Table 2. As $\hat{H}_w > 1/\hat{\alpha}$ and $\hat{H}_b \ll 1/\hat{\alpha}$
317 in all cases, we conclude that whereas intra-layer variability is persistent (large values tend to
318 follow large values and small values tend to follow small values), inter-layer variability is
319 strongly antipersistent (small and large values tend to alternate rapidly). The latter is likely a
320 manifestation of strong variations in environments responsible for the deposition of alternating
321 sedimentary layers.

322 As no theory other than ours (Siena et al., 2012; Neuman et al., 2013) is known to explain
 323 extended self-similarity (ESS) of variables that do not necessarily satisfy Burger's equation
 324 (Chakraborty et al., 2010), demonstrating that $\Delta P(s_n)$ satisfy ESS is akin to verifying that these
 325 data conform to our theoretical scaling framework. That this is indeed the case becomes evident
 326 upon examining the high-confidence ($R^2 = 0.91 - 0.99$) straight line relationships between log
 327 S_N^{q+1} and $\log S_N^q$, and corresponding power-law relationships between S_N^{q+1} and S_N^q , at $s_n < 10$
 328 and $s_n > 12$ in Figure 8 for $q = 1, 2$ and 3 in Wells 1 (Maroon) and 6 (Tabnak). Similar ESS
 329 relationships hold (not shown) in Wells 2 - 5.

330 Our next step is to compute functional relationships between power exponents $\xi_w(q)$ and
 331 $\xi_b(q)$, and the order q , of structure functions that scale as power-laws of lag. In the method of
 332 moments these powers are the slopes of regression lines fitted to log-log plots of $S_N^q(s_n)$ versus
 333 s_n , such as those depicted in Figure 7. In the case of ESS we use $\xi_w(q = 1)$ and $\xi_b(q = 1)$,
 334 determined by the method of moments, as reference values for the sequential computation of
 335 $\xi_w(q)$ and $\xi_b(q)$ at $q > 1$ based on known power-law relationships between S_N^{q+1} and S_N^q , such as
 336 those given in Figure 8. Corresponding plots of $\xi_w(q)$ and $\xi_b(q)$ as functions of q , evaluated by
 337 the method of moments and ESS in Wells 1 and 6 at $s_n < 10$ and $s_n > 12$, are presented in Figure
 338 9. Results obtained by the two methods are, for the most part, very similar. With the exception of
 339 $\xi_w(q)$ at $s_n < 10$ in Wells 1, 2, and 3 (Maroon field), in all cases (including those corresponding to
 340 Wells 2 - 5, which we do not show) $\xi_w(q)$ and $\xi_b(q)$ delineate convex functions that fall below
 341 straight lines having slopes \hat{H}_w and \hat{H}_b , respectively, which pass through the origin. Tradition
 342 has it that whereas such straight lines are characteristic of monofractal (self-affine, additive)
 343 random fields, nonlinear variations of power exponents such as those exhibited by $\xi_w(q)$ and

344 $\xi_b(q)$ in Figure 9 are symptomatic of (multiplicative) multifractals. Yet we have seen that the data
 345 in this paper conform to a statistical scaling theory in which the underlying random fields are
 346 subordinated to truncated versions of monofractal fBm or fGn. As we have previously
 347 demonstrated theoretically (Neuman, 2010, 2011; Neuman et al., 2013) and computationally
 348 (Guadagnini et al., 2012), nonlinear scaling of such data is nothing but a random artifact of
 349 sampling from similar fields.

350 7. ESTIMATION OF VARIOGRAM PARAMETERS

351 We saw that our analysis supports treating the neutron porosity data from each well as a
 352 random sample from a stationary sub-Gaussian random field subordinated to tfBm or tfGn. Our
 353 previous ML fits of univariate α -stable and NLN pdf models to neutron porosity increments in
 354 each well have yielded estimates of all distributional parameters characterizing these models. We
 355 also found the data to exhibit different modes of scaling at $s_n < 10$ and $s_n > 12$ and obtained
 356 estimates of H for each of these two ranges of lags. All that remains to fully characterize the
 357 multivariate random fields, $\Delta Y(x, x+s; \lambda_l, \lambda_u)$, which we take to underlie the incremental data
 358 is to estimate the parameters A , λ_l and λ_u (and, optionally, H) of TPVs corresponding to $s_n < 10$
 359 and $s_n > 12$. We do so next for each of the two subordinators we consider.

360 Assuming first that neutron porosity increments in each well are α -stable, one can
 361 estimate the scale parameter $\sigma(s; \lambda_l, \lambda_u)$ of their distribution at any lag, s , from the theoretical
 362 relationship (Samorodnitsky and Taqqu, 1994)

$$363 \hat{\sigma}(s; \lambda_l, \lambda_u) = \sqrt{\gamma_G(s; \lambda_l, \lambda_u)}. \quad (9)$$

364 Here we employ this relationship separately for normalized lag ranges $s_n < 10$ and $s_n > 12$. We
 365 saw earlier that structure functions of neutron porosity data in both lag ranges, including second-

366 order structure functions can be closely represented in each well by power laws. In other words,
 367 the TPVs within these lag ranges are effectively PVs. We recall that this happens in the limits as
 368 λ_l and λ_u tend, respectively, to zero and infinity. We note further that λ_l should be a fraction of
 369 the measurement scale. In our case, the measurement scale can be considered as smaller than the
 370 0.15 m data resolution scale (in Well 6 data resolution is 0.07 m). When compared to the much
 371 larger length scale of each borehole (on the order of 10^3 m), λ_l is negligibly small and can be
 372 disregarded. Accordingly, we set $\lambda_l = 0$ and λ_u to a sufficiently large number to ensure that the
 373 TPV $\gamma_G(s; \lambda_l, \lambda_u)$ reduces, within both working lag ranges, to the PV $\gamma^2(s) = Bs^{2H}$. Then, in a
 374 manner analogous to that outlined most recently by Guadagnini et al. (2013, 2014), we obtain
 375 ML estimates \hat{A} of A in two ways, once by adopting corresponding method-of-moment estimates
 376 \hat{H}_w and \hat{H}_b from Table 2 and once by estimating the latter jointly with A . Both sets of estimates
 377 are obtained upon fitting the theoretical PV $\gamma^2(s) = Bs^{2H}$ to sample scale parameters $\hat{\sigma}(s_n)$
 378 such as those plotted versus s_n in Figure 7b. The fits are depicted graphically in Figure 10 for
 379 Wells 1 and 6. The corresponding parameter estimates and 95% confidence limits are listed, for
 380 all wells and both lag ranges, in Table 3. The two sets of estimates lie within each other's 95%
 381 confidence intervals, implying that they are equally reliable.

382 Next we consider the case where neutron porosity increments in each well are NLN. Due
 383 to finiteness of all (statistical) moments associated with this model, structure functions of order q
 384 $= 2$ in Figure 7 coincide with twice the variogram of neutron porosity. As shown in Appendix A,
 385 the variogram of $Y'(x; \lambda_l, \lambda_u)$ is given by

$$386 \gamma_Y(s_n; \lambda_l, \lambda_u) = \left(\mu_W^2 + \sigma_W^2 \right) \gamma_G(s_n; \lambda_l, \lambda_u) \tag{10}$$

387 where μ_w and σ_w^2 are defined in (A1). We replace (10) by $\gamma_Y(s) = Cs^{2H}$ and fit the latter by
388 ML to second-order sample structure functions of porosity increments in each well, separately
389 for $s_n < 10$ and $s_n > 12$. Joint estimates of C and H for each range of lags, as well as ML
390 estimates of C based on method-of-moment estimates \hat{H}_w and \hat{H}_b from Table 2, together with
391 associated 95% confidence intervals, are listed in Table 4. Corresponding best fits are depicted
392 graphically in Figure 11. Here again the two sets of estimates lie within each other's 95%
393 confidence intervals, implying that they are equally reliable.

394 **8. FREQUENCY DISTRIBUTIONS OF PEAKS OVER THRESHOLDS**

395 Extreme value analyses of randomly varying data typically concern block maxima (BM)
396 and/or peaks over thresholds (POTs). The number of neutron porosity increments, $\Delta P(s_n)$,
397 available to us at any normalized lag at any well are insufficient to conduct a statistically
398 meaningful analysis of BM. For this reason, and for the fact that POTs provide a higher
399 resolution of maxima than do BM, we focus in this paper exclusively on the former. In way of
400 illustration we consider absolute increments $|\Delta P(s_n)|$ to constitute POTs whenever they exceed a
401 non-negative threshold, u_t , equal to the 95% quantile of $|\Delta P(s_n)|$ values in a sample. This
402 renders about 5% of all sampled $|\Delta P(s_n)|$ values POTs. Figure 12 identifies POTs associated
403 with sequences of porosity increments depicted in Figure 3.

404 In each well, sample autocorrelation of non-overlapping neutron porosity increments at
405 diverse normalized lags diminishes rapidly with the number, n , of these normalized increments
406 (not shown), in line with theoretical expressions (18) - (20) of Neuman (2010). We expect
407 autocorrelations between POTs to be weaker, possibly justifying a representation of their
408 frequency distributions by generalized Pareto distributions (GPDs, see Appendix B) which,

409 theoretically, apply to independent identically distributed (iid) variables. To test this, we plot in
410 Figure 13 quantile-quantile (Q-Q) plots of GPD fits to frequency distributions of POTs identified
411 in Figure 12. Included in Figure 13 are 95% confidence intervals of these fits and p -values of
412 Kolmogorov-Smirnov (KS) goodness-of-fit tests. A list of POT sample sizes and p -values
413 associated with the same three lags in all wells is provided in Table 5. The p -value is the
414 probability of obtaining given data when a null hypothesis is true. As all p -values in Table 5
415 exceed 0.05, one cannot reject (at a significance level of 0.05) the null hypothesis that all POTs
416 have GPDs.

417 Figure 14 shows variations of best fit GPD shape (ζ_{POT} , governing the tail behavior of the
418 distribution) and scale (σ_{POT} , governing the spread of the distribution) parameters with
419 normalized lag, and corresponding 95% uncertainty bounds, in the same wells as in Figure 13.
420 With the exception of Well 6 in which ζ_{POT} first diminishes with lag and then stabilizes, this
421 parameter fluctuates but does not vary systematically with lag. The same applies to the shape
422 parameter of each fitted GPD. On the other hand σ_{POT} in all wells increases as a power of lag
423 before stabilizing at larger lags, as does the scale parameter of α -stable distributions fitted to all
424 neutron porosity increments in Figure 6b.

425 9. STATISTICAL SCALING OF PEAKS OVER THRESHOLDS

426 We end our analysis by exploring the scaling behavior of q -order sample structure
427 functions of POT in absolute increments $|\Delta P_{POT,j}(s_n)|$. Following Equation (1), these sample
428 structure functions are defined as

$$429 S_{N_{POT}}^q(s_n) = \frac{1}{N_{POT}(s_n)} \sum_{j=1}^{N_{POT}(s_n)} |\Delta P_{POT,j}(s_n)|^q \quad (11)$$

430 where $N_{POT}(s_n)$ is the number of POTs at normalized lag s_n . We do so as we did earlier for all
431 increments, according to the methodology summarized in Section 3. Figure 15 depicts variations
432 of $S_{N_{POT}}^q(s_n)$ with normalized lag for $q = 0.5, 1.0, \text{ and } 2.0$ in Wells 1 (Maroon) and 6 (Tabnak). A
433 red dashed line in the figure demarcates cross-over between two diverse power-law scaling
434 regimes at $s_n < 10$ and $s_n > 12$. Included in Figure 15 are logarithmic scale regression lines and
435 corresponding power-law relations between $S_{N_{POT}}^q(s_n)$ and s_n in each well and scaling regime.
436 The scaling behavior in Figure 15 is similar to that shown previously for all (unfiltered) porosity
437 increments in Figure 7. Corresponding estimates of Hurst exponent are listed in Table 6; these
438 too differ little from those obtained earlier for all porosity increments (Table 2) with the
439 exception of estimates \hat{H}_b which are consistently lower than those associated with unfiltered
440 increments. Like the latter (Figure 8), POTs exhibit ESS at all lags in the scaling intervals $s_n < 10$
441 and $s_n > 12$ (not shown).

442 Our final step is to compute functional relationships between power exponents $\xi_w(q)$ and
443 $\xi_b(q)$, and the order q , of POT structure functions that scale as power-laws of lag. We do so as we
444 did previously for unfiltered porosity increments. Corresponding plots of $\xi_w(q)$ and $\xi_b(q)$ as
445 functions of q , evaluated by the method of moments and ESS in Wells 1 and 6 at $s_n < 10$ and $s_n >$
446 12 , are presented in Figure 16. Results obtained by the two methods are again, for the most part,
447 very similar. Similar behavior has been shown by us elsewhere (Guadagnini et al., 2012) to be
448 consistent with increments sampled from random fields subordinated to tfBm or tfGn.

449 10. CONCLUSIONS

450 After showing that neutron porosity data from six deep boreholes in three geologic
451 environments have statistical scaling properties characteristic of samples from scale-mixtures of
452 truncated fractional Brownian motion (tfBm) or fractional Gaussian noise (tfGn), we used these

453 data to explore the statistical behavior of extreme porosity increments the absolute values of
454 which exceed certain thresholds. We expect our results to hold for many earth, environmental
455 and other variables that were shown elsewhere to possess similar statistical scaling properties.
456 These results include the following:

- 457 1. The frequency distributions of neutron porosities in any well, or group of wells in any
458 one of the three geologic environments, are non-Gaussian with sharp peaks, asymmetry
459 and slight bimodality.
- 460 2. The frequency distributions of neutron porosity increments in any well, or group of wells
461 at one of the three sites, are zero-mean symmetric with heavy tails that decay with
462 increasing vertical separation distance or lag. At all lags, the distributions are represented
463 closely by either α -stable or normal-log-normal probability density models that tend to
464 Gaussian with increasing lag.
- 465 3. Order q structure functions of absolute neutron porosity increments grow approximately
466 as positive powers $\xi_w(q)$ of normalized lag, s_n , at $s_n < 10$ and as much smaller positive
467 powers, $\xi_b(q)$, of s_n at $s_n > 12$. We interpret this dual power-law scaling to represent
468 within- or intra-layer variability at $s_n < 10$ and between- or inter-layer variability at $s_n >$
469 12. Values of $\xi_w(q=1)$ and $\xi_b(q=1)$ provide method-of-moment estimates of Hurst
470 exponents H_w and H_b for these two power-law scaling ranges, respectively.
- 471 4. Structure functions of absolute neutron porosity increments exhibit extended self
472 similarity (ESS) at all normalized lags within both power-law scaling ranges, $s_n < 10$ and
473 $s_n > 12$.

474 5. Values of power-law exponents $\xi_w(q)$ and $\xi_b(q)$ associated with absolute neutron porosity
475 data, computed by the method of moments and by ESS, are for the most part very similar.
476 Whereas such nonlinear scaling of power-law exponents has traditionally been viewed as
477 a hallmark of multifractality (or, more recently, of fractional Laplace motion), we find the
478 neutron porosity data in this paper to behave in a way fully consistent with that of
479 samples from sub-Gaussian random fields subordinated to truncated (monofractal, self-
480 affine, Gaussian) fractional Brownian motion or fractional Gaussian noise. The latter is
481 the only view known to be theoretically consistent with ESS in the case of data, such as
482 those considered here, that do not necessarily satisfy Burger's equation.

483 6. Our method of interpretation allows one to fully characterize the sub-Gaussian random
484 field that underlies a given set of data by estimating the parameters of corresponding
485 (generally truncated) power variograms.

486 7. The autocorrelation of neutron porosity increments diminishes rapidly with the number,
487 n , of non-overlapping increments in a separation distance (lag). This helps explain why
488 sample distributions of peaks over thresholds (POTs, taken here to be absolute
489 increments which exceed their 95% quantile) are described reasonably well by a
490 generalized Pareto distribution (GPD) model, which in theory applies to independent
491 identically distributed (iid) extrema. Whereas GPD shape parameter estimates do not
492 show systematic variations with lag except in one well, corresponding estimates of GPD
493 shape parameters tend to increase as a power of small lags and stabilize at larger lags.
494 The same happens with scale parameters of α -stable distributions fitted to all
495 (unfiltered) neutron porosity increments.

496 8. In all other respects, POTs show statistical scaling very similar to that of unfiltered
497 increments. Estimates of POT Hurst exponents are very close to those obtained for
498 unfiltered increments, with the exception of \hat{H}_b that are consistently lower than those
499 associated with unfiltered increments. Such nonlinear scaling is consistent with our
500 method of interpreting the data. To our knowledge, this is the first documented example
501 of POT statistical scaling interpreted on the basis of sub-Gaussian theory. We are not
502 aware of any known theoretical reason why statistics of POT increments would
503 necessarily scale in a manner similar to that of their parent population, as they do here.
504

APPENDIX A

505

506

Let $\Delta Y(x, x+s) = W^{1/2} \Delta G(x, x+s)$ where x is a spatial (or temporal) coordinate, $s \geq 0$ is

507

lag, $W^{1/2}$ is a random variable acting as subordinator, and ΔG is a zero-mean Gaussian random

508

field of increments with pdf $f_{\Delta G}(\Delta g)$ and variance $\sigma_{\Delta G}^2$ dependent on lag, ΔG and $W^{1/2}$ being

509

statistically independent of each other at all lags. In this paper we consider W to be either Lévy

510

stable or lognormal.

511

In the first case (e.g., Samorodnitsky and Taquq, 1994) W is $\alpha/2$ -stable totally skewed to

512

the right of zero (hence non-negative) with scale parameter $\sigma_s = (\cos \frac{\pi\alpha}{4})^{2/\alpha}$, unit skewness and

513

zero shift. The corresponding pdf of ΔY is symmetric α -stable with zero skewness and shift. In

514

the second case we follow Neuman (2011) and Guadagnini et al. (2012) by setting $W^{1/2} = e^V$

515

where V is zero-mean Gaussian with variance $\sigma_V^2 = (2-\alpha)^2$, yielding the following respective

516

mean and variance expressions for $W^{1/2}$,

517

$$\mu_W = \exp(\sigma_V^2 / 2) \quad \text{and} \quad \sigma_W^2 = \exp(\sigma_V^2) [\exp(\sigma_V^2) - 1] \quad (\text{A1})$$

518

Correspondingly, the pdf of ΔY is

519

$$f_{\Delta Y}(\Delta y) = \int_{-\infty}^{\infty} \frac{1}{|u|} f_U(u) f_{\Delta G}\left(\frac{\Delta y}{u}\right) du \quad (\text{A2})$$

520

where $U = W^{1/2}$, $u = w^{1/2}$. Since $U = W^{1/2} > 0$ one has

521

$$f_{\Delta Y}(\Delta y) = \int_0^{\infty} \frac{1}{u} f_U(u) f_{\Delta G}\left(\frac{\Delta y}{u}\right) du. \quad (\text{A3})$$

522

As $\Delta G \sim N(0, \sigma_{\Delta G}^2)$ and $U = W^{1/2} \sim \ln N(0, \sigma_V^2)$, Equation (A3) becomes

523
$$f_{\Delta Y}(\Delta y) = \frac{1}{2\pi\sigma_V} \int_0^\infty \frac{1}{u^2} e^{-\frac{\Delta y^2}{2u^2}} \cdot e^{-\frac{(\ln u - \ln \sigma_{\Delta G})^2}{2\sigma_V^2}} du . \quad (\text{A4})$$

524 This is the normal-log-normal (NLN) pdf we refer to in the text. In it $\sigma_{\Delta G}$ plays the role of a
 525 scale parameter, and σ_V of a shape factor. Letting $\sigma_V \rightarrow 0$ is tantamount to letting Equation

526 (A4) converge to a Normal density $f_{\Delta Y}(\Delta y) = \frac{1}{\sqrt{2\pi}\sigma_{\Delta G}} e^{-\frac{(\Delta y)^2}{2\sigma_{\Delta G}^2}}$. The larger is σ_V the heavier are

527 the tails and the sharper is the peak of the NLN distribution. Fitting Equation (A4) by maximum
 528 likelihood (ML) to sample frequency distributions of ΔY allows one to estimate $\sigma_{\Delta G}^2$ and σ_V^2 ,
 529 which in turn allows one to estimate μ_W and σ_W^2 according to Equation (A1). The variance of

530 ΔY is $\sigma_{\Delta Y}^2 = (\mu_W^2 + \sigma_W^2)\sigma_{\Delta G}^2$ -and the variogram of Y' is

531
$$\gamma_Y(s) = \frac{1}{2} E[(\Delta Y(x, s))^2] = E[(W^{1/2})^2] \cdot \frac{1}{2} E[(\Delta G(x, s))^2] = (\sigma_W^2 + \mu_W^2) \gamma_G(s) \quad (\text{A5})$$

532 where $\gamma_G(s)$ is the variogram of G' . Once μ_W and σ_W^2 have been estimated by maximum
 533 likelihood on the basis of ΔY data as described above, fitting (A5) to corresponding second-
 534 order sample structure functions allows one to estimate all parameters of $\gamma_G(s)$.

535 In case G' has a power variogram, $\gamma_G(s) = Bs^{2H}$, of the kind we consider in the
 536 manuscript so does Y ,

537
$$\gamma_Y(s) = (\sigma_W^2 + \mu_W^2) \gamma_G(s) = Cs^{2H} . \quad (\text{A6})$$

538 where C is a coefficient. Fitting Equation (A6) to second-order sample structure functions of
 539 corresponding increments allows one to estimate C and H .

540 **APPENDIX B**

541 In this work empirical distributions of POTs of absolute neutron porosity increments at
 542 normalized lag s_n , $|\Delta P(s_n)|$, are shown to fit well-known two-parameter Generalized Pareto
 543 distributions (GPDs). A GPD is described in terms of the following cumulative distribution
 544 function (CDF)

$$545 \quad H(y) = 1 - \left(1 + y \zeta_{POT} / \sigma_{POT}\right)^{-1/\zeta_{POT}} ; \quad y = |\Delta P(s_n)| - u_t > 0 \quad (B1)$$

546 where ζ_{POT} and σ_{POT} are the shape and scale parameters, respectively, governing tail behavior
 547 and spread of the distribution; u_t is the predetermined threshold. Equation (B1) reduces to a
 548 Pareto (type-II) distribution when $\zeta_{POT} > 0$, an exponential distribution when $\zeta_{POT} = 0$ and a
 549 generalized Beta distribution (of the first kind) when $\zeta_{POT} < 0$ (Arnold, 2008).

550

551
552
553
554
555
556
557
558
559

ACKNOWLEDGEMENTS

This work was supported in part through a contract between the University of Arizona and Vanderbilt University under the Consortium for Risk Evaluation with Stakeholder Participation (CRESP) III, funded by the U.S. Department of Energy. Funding from MIUR (Italian ministry of Education, Universities and Research- PRIN2010-11; project: "Innovative methods for water resources under hydro-climatic uncertainty scenarios") is also acknowledged. We thank Professor Muhammad Sahimi, University of Southern California, for having generously shared with us borehole geophysical log data some of which we analyze in this paper.

REFERENCES

- 560
- 561 Akaev, A., Sadovnichy, V., and Korotayev, A.: On the dynamics of the world demographic
562 transition and financial-economic crises forecasts, *Eur. Phys. J.-Special Topics*, 205, 355-
563 373, doi:10.1140/epjst/e2012-01578-2, 2012.
- 564 Amitrano, D.: Variability in the power-law distributions of rupture events, *Eur. Phys. J.-Special*
565 *Topics*, 205, 199-215, doi:10.1140/epjst/e2012-01571-9, 2012.
- 566 Ancey, C.: Are there “dragon-kings” events (i.e. genuine outliers) among extreme avalanches?,
567 *Eur. Phys. J.-Special Topics*, 205, 117-129, doi:10.1140/epjst/e2012-01565-7, 2012.
- 568 Andrews, D. F. and Mallows, C.L.: Scale Mixtures of Normal Distributions, *J. Roy. Stat. Soc. B*
569 *Met.*, 36, 99-102, <http://www.jstor.org/stable/2984774>, 1974.
- 570 Arnold, B. C.: Pareto and Generalized Pareto Distributions, in: *Modeling Income Distributions*
571 *and Lorenz Curves*, Chotikapanich, D. (Ed.), Springer Science & Business Media, New
572 York NY, 119-145, 2008.
- 573 Barrash, W., and Reboulet, E.C.: Significance of porosity for stratigraphy and textural
574 composition in subsurface coarse fluvial deposits, Boise Hydrogeophysical Research Site,
575 *Geological Society of America Bulletin*, 116(9-10), 1059-1073, doi:10.1130/B25370.1,
576 2004.
- 577 Benzi, R., Ciliberto, S., Baudet, C., Chavarria, G. R., and Tripiccone, R.: Extended self-
578 similarity in the dissipation range of fully developed turbulence, *Europhys. Lett.*, 24(4),
579 275-279, 1993a.
- 580 Benzi, R., Ciliberto, S., Tripiccone, R., Baudet, C., Massaioli, F., and Succi, S.: Extended self-
581 similarity in turbulent flows, *Phys. Rev. E*, 48, R29-R32, 1993b.

582 Benzi, R., Biferale, L., Ciliberto, S., Struglia, M. V., and Tripiccione, R.: Generalised scaling in
583 fully developed turbulence, *Phys. D*, 96, 162-181, 1996.

584 Burlando, P., and Rosso, R.: Scaling and multiscaling models of depth-duration-frequency
585 curves for storm precipitation, *J. Hydrol.*, 187, 45-64, doi:10.1016/S0022-1694(96)03086-
586 7, 1996.

587 Castro, J. J., Carsteanu, A. A., and Flores, C. G.: Intensity-duration-area-frequency functions for
588 precipitation in a multi-fractal framework, *Physica A*, 338, 206-210,
589 doi:10.1016/j.physa.2004.02.043, 2004.

590 Chakraborty, S., Frisch, U., and Ray, S. S.: Extended self-similarity works for the Burgers
591 equation and why, *J. Fluid Mech.*, 649, 275-285, doi:1017/S0022112010000595, 2010.

592 Dashtian, H., Jafari, G. R., Sahimi, M., and Masihi, M.: Scaling, multifractality, and long-range
593 correlations in well log data of large-scale porous media, *Physica A*, 390, 2096-2111,
594 doi:10.1016/j.physa.2011.01.010, 2011.

595 de Arcangelis, L.: Are dragon-king neuronal avalanches dungeons for self-organized brain
596 activity?, *Eur. Phys. J.-Special Topics*, 205, 243-257, doi:10.1140/epjst/e2012-01574-6,
597 2012.

598 De Michele, C., Kottegoda, N. T., and Rosso, R.: The derivation of areal reduction factor of
599 storm rainfall from its scaling properties, *Water Resour. Res.*, 37(12), 3247-3252,
600 doi:10.1029/2001WR000346, 2001.

601 Di Federico, V., and Neuman, S. P.: Scaling of random fields by means of truncated power
602 variograms and associated spectra, *Water Resour. Res.*, 33, 1075-1085,
603 doi:10.1029/97WR00299, 1997.

604 Ebtehaj, M. and Foufoula-Georgiou, E.: Orographic signature on multiscale statistics of extreme
605 rainfall: A storm-scale study, *J. Geophys. Res.-Atmos.*, 115, doi:10.1029/2010JD014093,
606 2010.

607 Embrechts, P., Mikosch, T., and Klüppelberg, C.: *Modelling Extremal Events For Insurance and*
608 *Finance*, Springer-Verlag, London, UK, 1997.

609 Fogg, G. E., Carle, S. F., and Green, C.: Connected-network paradigm for the alluvial aquifer
610 system. In: *Theory, Modeling, and Field Investigation in Hydrogeology: A Special*
611 *Volume in Honor of Shlomo P. Neuman's 60th Birthday*, Zhang, D. and Winter, C.L.
612 (Eds.), Geological Society of America Special Paper 348, Boulder, Colorado, 25-42, 2000.

613 Frisch, U.: *Turbulence*, Cambridge University Press, Cambridge, 1995.

614 Garcia-Bartual, R., and Schneider, M.: Estimating maximum expected short-duration rainfall
615 intensities from extreme convective storms, *Phys. Chem. Earth Pt. B*, 26, 675-681,
616 doi:10.1016/S1464-1909(01)00068-5, 2001.

617 Golosovsky, M., and Solomon, S.: Runaway events dominate the heavy tail of citation
618 distributions, *Eur. Phys. J.-Special Topics*, 205, 303-311, doi:10.1140/epjst/e2012-01576-
619 4, 2012.

620 Gómez-Hernández, J. J., and Wen, X.-H.: To be or not to be multi-Gaussian. A reflection on
621 stochastic hydrogeology, *Advances Water Resour.*, 21(1), 47-61, doi:10.1016/S0309-
622 1708(96)00031-0, 1998.

623 Guadagnini, A., and Neuman, S. P.: Extended power-law scaling of self-affine signals
624 exhibiting apparent multifractality, *Geophys. Res. Lett.*, 38, doi:10.1029/2011gl047727,
625 2011.

626 Guadagnini, A., Neuman, S. P., and Riva, M.: Numerical investigation of apparent
627 multifractality of samples from processes subordinated to truncated fBm, *Hydrol. Proc.*,
628 26, 2894-2908, doi:10.1002/Hyp.8358, 2012.

629 Guadagnini, A., Neuman, S. P., Schaap, M. G., and Riva, M.: Anisotropic statistical scaling of
630 vadose zone hydraulic property estimates near Maricopa, Arizona, *Water Resour. Res.*, 49,
631 8463-8479, doi:10.1002/2013wr014286, 2013.

632 Guadagnini, A., Neuman, S. P., Schaap, M. G., and Riva, M.: Anisotropic statistical scaling of
633 soil and sediment texture in a stratified deep vadose zone near Maricopa, Arizona,
634 *Geoderma*, 214, 217-227, doi:10.1016/j.geoderma.2013.09.008, 2014.

635 Janczura, J. and Weron, R.: Black swans or dragon-kings? A simple test for deviations from the
636 power law, *Eur. Phys. J.-Special Topics*, 205,79-93, doi:10.1140/epjst/e2012-01563-9,
637 2012.

638 Javelle, P., Gresillon, J. M., and Galea, G.: Discharge-duration-frequency curve modelling for
639 floods and scale invariance, *Comptes Rendus De L Academie Des Sciences Serie Ii*
640 *Fascicule a-Sciences De La Terre Et Des Planetes*, 329, 39-44, doi:10.1016/S1251-
641 8050(99)80225-0, 1999.

642 Kashyap, R.L., Optimal choice of AR and MA parts in autoregressive moving average models,
643 *IEEEET Pattern. Anal.* 4(2), 99-104, 1982.

644 Katz, R. W., Parlange, M. B., and Naveau, P.: Statistics of extremes in hydrology, *Adv. Water*
645 *Resour.*, 25, 1287-1304, doi:10.1016/S0309-1708(02)00056-8, 2002.

646 Knudby, C., and Carrera, J.: On the relationship between indicators of geostatistical, flow and
647 transport connectivity, *Adv. Water Resour.* 28, 405-421, doi:
648 10.1016/j.advwatres.2004.09.001, 2005.

649 Knudby, C., Carrera, J.: On the use of apparent hydraulic diffusivity as an indicator of
650 connectivity. *J. Hydrol.* 329, 377-389, doi:10.1016/j.jhydrol.2006.02.026, 2006.

651 Knudby, C., Carrera, J., Bumgardner, J. D., and Fogg, G. E.: Binary upscaling - the role of
652 connectivity and a new formula, *Adv. Water Resour.* 29, 590-604, 2006.

653 Kozubowski, T. J., Meerschaert, M. M., and Podgorski, K.: Fractional Laplace motion, *Adv.*
654 *Appl. Probab.* 38, 451-464, doi:10.1239/aap/1151337079, 2006.

655 Langousis, A. and Veneziano, D.: Intensity-duration-frequency curves from scaling
656 representations of rainfall, *Water Resour. Res.*, 43, doi:10.1029/2006wr005245, 2007.

657 Lei, X.: Dragon-Kings in rock fracturing: Insights gained from rock fracture tests in the
658 laboratory, *Eur. Phys. J.-Special Topics*, 205, 217-230, doi:10.1140/epjst/e2012-01572-8,
659 2012.

660 Main, I., and Naylor, M.: Extreme events and predictability of catastrophic failure in composite
661 materials and in the Earth, *Eur. Phys. J.-Special Topics*, 205, 183-197,
662 doi:10.1140/epjst/e2012-01570-x, 2012.

663 Mariethoz, G., and Renard, P.: Special Issues on 20 years of multiple-point statistics: part 2,
664 *Math. Geosc.*, 46, 517-518, doi:10.1007/s11004-014-9545-y, 2014.

665 Meerschaert, M. M., Kozubowski, T. J., Molz, F. J., and Lu, S.: Fractional Laplace model for
666 hydraulic conductivity, *Geophys. Res. Lett.*, 31, L08501, doi:10.1029/2003GL019320,
667 2004.

668 Meier, P. M., Carrera, J., and Sanchez-Vila, X.: An evaluation of Jacob's method for the
669 interpretation of pumping tests in heterogeneous formations, *Water Resour. Res.*, 34(5),
670 1011-1025, doi:10.1029/98WR00008, 1998.

671 Menabde, M., Seed, A., and Pegram, G.: A simple scaling model for extreme rainfall, *Water*
672 *Resour. Res.*, 35, 335-339, doi:10.1029/1998wr900012, 1999.

673 Menabde, M., and Sivapalan, M.: Linking space-time variability of river runoff and rainfall
674 fields: a dynamic approach, *Adv. Water Resour.*, 24, 1001-1014, doi:10.1016/S0309-
675 1708(01)00038-0, 2001.

676 Mohyont, B., and Demarée, G. R.: Intensity-duration-frequency curves for precipitation at
677 Yangambi, Congo, derived by means of various models of Montana type, *Hydrolog. Sci.*
678 *J.*, 51(2), 239-253, doi: 10.1623/hysj.51.2.239, 2006.

679 Neuman, S. P.: Apparent/spurious multifractality of absolute increments sampled from
680 truncated fractional Gaussian/Levy noise, *Geophys. Res. Lett.*, 37,
681 doi:10.1029/2010gl043314, 2010.

682 Neuman, S. P.: Apparent multifractality and scale-dependent distribution of data sampled from
683 self-affine processes, *Hydrol. Process.*, 25, 1837-1840, doi:10.1002/Hyp.7967, 2011.

684 Neuman, S. P., Guadagnini, A., Riva, M., and Siena, M.: Recent advances in statistical and
685 scaling analysis of earth and environmental variables, in: *Advances in Hydrogeology*,
686 edited by Mishra, P. K. and Kuhlman, K. L., Springer, New York, 2013.

687 Nguyen, V. T. V., Nguyen, T. D., and Wang, H.: Regional estimation of short duration rainfall
688 extremes, *Water Sci. Technol.*, 37, 15-19, doi:10.1016/S0273-1223(98)00311-4, 1998.

689 Nield, D. A.: Connectivity and Effective Hydraulic Conductivity, *Transp. Porous Med.*, 74,
690 129-132, doi:10.1007/s11242-007-9185-5, 2008.

691 Nolan, J.: Maximum likelihood estimation of stable parameters, in: *Lévy Processes: Theory and*
692 *Applications*, edited by Barndorff-Nielsen, O., Mikosch, T., and Resnick, S., Birkhauser,
693 Boston, 2001.

694 Painter, S.: Flexible scaling model for use in random field simulation of hydraulic conductivity,
695 Water Resour. Res. 37, 1155-1163, 2001.

696 Pisarenko, V. F., and Sornette, D.: Robust statistical tests of Dragon-Kings beyond power law
697 distributions, Eur. Phys. J.-Special Topics, 205, 95-115, doi:10.1140/epjst/e2012-01564-8,
698 2012.

699 Plenz, D.: Neuronal avalanches and coherence potentials, Eur. Phys. J.-Special Topics, 205,
700 259-301, doi:10.1140/epjst/e2012-01575-5, 2012.

701 Renard, P., and Mariethoz, G.: Special Issues on 20 years of multiple-point statistics: part 1,
702 Math. Geosc., 46, 129-131, doi:10.1007/s11004-014-9524-3, 2014.

703 Rigon, R., D'Odorico, P., and Bertoldi, G.: The geomorphic structure of the runoff peak,
704 Hydrol. Earth Syst. Sci., 15, 1853-1863, doi:10.5194/hess-15-1853-2011, 2011.

705 Riva, M., Neuman, S. P., and Guadagnini, A.: On the identification of Dragon Kings among
706 extreme-valued outliers, Nonlinear Proc. Geoph., 20, 549-561, doi:10.5194/npg-20-549-
707 2013, 2013a.

708 Riva, M., Neuman, S. P., Guadagnini, A., and Siena, M.: Anisotropic scaling of berea sandstone
709 log air permeability statistics, Vadose Zone J., 12, doi:10.2136/Vzj2012.0153, 2013b.

710 Riva, M., Neuman, S. P., and Guadagnini, A.: Sub-Gaussian model of processes with heavy-
711 tailed distributions applied to air permeabilities of fractured tuff, Stoch. Env. Res. Risk A.,
712 27, 195-207, doi:10.1007/s00477-012-0576-y, 2013c.

713 Riva, M., Sanchez-Vila, X., and Guadagnini, A.: Estimation of spatial covariance of log
714 conductivity from particle size data, Water Resour. Res., 50(6), 5298-5308,
715 doi:10.1002/2014WR015566, 2014.

716 Sachs, M., Yoder, M., Turcotte, D., Rundle, J., and Malamud, B.: Black swans, power laws, and
717 dragon-kings: Earthquakes, volcanic eruptions, landslides, wildfires, floods, and SOC
718 models, *Eur. Phys. J.-Special Topics*, 205, 167-182, doi:10.1140/epjst/e2012-01569-3,
719 2012.

720 Samorodnitsky, G., and Taqqu, M. S.: *Stable Non-Gaussian Random Processes*, Chapman and
721 Hall, New York, 1994.

722 Sanchez-Vila, X., Carrera, J., and Girardi, J. P.: Scale effects in transmissivity, *J. Hydrol.*, 183,
723 1-22, doi:10.1016/S0022-1694(96)80031-X, 1996.

724 Schertzer, D., and Lovejoy, S.: Physical Modeling and Analysis of Rain and Clouds by
725 Anisotropic Scaling Multiplicative Processes, *J. Geophys. Res.-Atmos.*, 92, 9693-9714,
726 doi: 10.1029/Jd092id08p09693, 1987.

727 Schoenberg, F., and Patel, R.: Comparison of Pareto and tapered Pareto distributions for
728 environmental phenomena, *Eur. Phys. J.-Special Topics*, 205, 159-166,
729 doi:10.1140/epjst/e2012-01568-4, 2012.

730 Siena, M., Guadagnini, A., Riva, M., and Neuman, S. P.: Extended power-law scaling of air
731 permeabilities measured on a block of tuff, *Hydrol. Earth Syst. Sci.*, 16, 29-42,
732 doi:10.5194/hess-16-29-2012, 2012.

733 Siena, M., Guadagnini, A., Riva, M., Bijeljic, B., Pereira Nunes, J. P., and Blunt, M. J.:
734 Statistical scaling of pore-scale Lagrangian velocities in natural porous media, *Phys. Rev.*
735 *E*, 90, 023013, doi:10.1103/PhysRevE.90.023013, 2014.

736 Süveges, M., and Davison, A.: A case study of a “Dragon-King”: The 1999 Venezuelan
737 catastrophe, *Eur. Phys. J.-Special Topics*, 205, 131-146, doi:10.1140/epjst/e2012-01566-6,
738 2012.

739 Trefry, C. M., Watkins, D. W., and Johnson, D.: Regional rainfall frequency analysis for the
740 state of Michigan, *J. Hydrol. Eng.*, 10, 437-449, doi:10.1061/(Asce)1084-
741 0699(2005)10:6(437), 2005.

742 Tronicke, J., and Holliger, K.: Quantitative integration of hydrogeophysical data: Conditional
743 geostatistical simulation for characterizing heterogeneous alluvial aquifers, *Geophysics*,
744 70(3), H1–H10, doi:10.1190/1.1925744, 2005.

745 Veneziano, D., and Furcolo, P.: Multifractality of rainfall and scaling of intensity-duration-
746 frequency curves, *Water Resour. Res.*, 38, doi:10.1029/2001WR000372, 2002.

747 Veneziano, D., Langousis, A., and Lepore, C.: New asymptotic and preasymptotic results on
748 rainfall maxima from multifractal theory, *Water Resour. Res.*, 45,
749 doi:10.1029/2009wr008257, 2009.

750 Veneziano, D., and Yoon, S.: Rainfall extremes, excesses, and intensity-duration-frequency
751 curves: A unified asymptotic framework and new nonasymptotic results based on
752 multifractal measures, *Water Resour. Res.*, 49, 4320-4334, doi:10.1002/wrcr.20352, 2013.

753 Vuković, M., and Soro, A.: Determination of hydraulic conductivity of porous media from
754 grain-size composition, *Water Resources Publications*, ISBN:0-918334-77-2, 1992.

755 Wen, X.-H., and Gómez-Hernández, J. J.: Numerical modeling of macrodispersion in
756 heterogeneous media - a comparison of multi-Gaussian and non-multi-Gaussian models, *J.*
757 *Contam. Hydrol.*, 30(1-2), 129-156, doi:10.1016/S0169-7722(97)00035-1, 1998.

758 West, M.: On scale mixtures of normal distributions, *Biometrika*, 74, 646-648,
759 doi:10.1093/biomet/74.3.646, 1987.

760 Western, A. W., Blöschl, G., and Grayson, R. B.: Toward capturing hydrologically significant
761 connectivity in spatial patterns, *Water Resour. Res.*, 37(1), 83-97,
762 doi:10.1029/2000WR900241, 2001.

763 Willems, P.: Compound intensity/duration/frequency-relationships of extreme precipitation for
764 two seasons and two storm types, *J. Hydrol.*, 233, 189-205, doi:10.1016/S0022-
765 1694(00)00233-X, 2000.

766 Yu, P. S., Yang, T. C., and Lin, C. S.: Regional rainfall intensity formulas based on scaling
767 property of rainfall, *J. Hydrol.*, 295, 108-123, doi:10.1016/j.jhydrol.2004.03.003, 2004.

768 Zinn, B., and Harvey, C. F.: When good statistical models of aquifer heterogeneity go bad: A
769 comparison of flow, dispersion, and mass transfer in connected and multivariate Gaussian
770 hydraulic conductivity fields, *Water Resour. Res.*, 39(3), 1051
771 doi:10.1029/2001WR001146, 2003.

772

773

774

Tables

775

776

Table 1: Summary information about available neutron porosity (P) data.

Reservoir	Well #	Sampling interval (m)	Min P (%)	Max P (%)	Mean P (%)	Standard Deviation SD (%)	Number of data points used
Maroon (MN)	1	0.1524	0	46.04	14	6.4	3,567
	2	0.1524	0*	74.29	17.27	9.98	4,049
	3	0.1524	0*	37.6	15.72	8.54	2,945
	1+2+3	0.1524	0*	74.29	15.74	8.62	10,561
Ahwaz (AZ)	4	0.1524	0	36.01	16.47	6.82	3,882
	5	0.1524	0	47.91	16.05	8.35	6,949
Tabnak (TBK)	6	0.0762**	0	96.9	9.28	13.2	4,267

777

* These, being negative and very close to zero, were set equal to zero.

778

** We disregard every other measurement in analyzing these data.

779

780

781

Table 2. Method of moments estimates of H for porosity increments at $s_n < 10$ (denoted by

782

subscript w) and $s_n > 12$ (subscript b).

Well	\hat{H}_w	\hat{H}_b
1 (Maroon field)	0.86	0.10
2 (Maroon field)	0.87	0.08
3 (Maroon field)	0.85	0.11
4 (Ahwaz field)	0.70	0.11
5 (Ahwaz field)	0.66	0.16
6 (Tabnak field)	0.75	0.17

783

784

785 Table 3. Estimates \hat{A} of A given estimates \hat{H} of H from Table 2, and joint estimates \hat{A}
786 and \hat{H} , of PVs with associated 95% confidence limits (in parenthesis) for all wells at $s_n < 10$ and
787 $s_n > 12$ in the case of α -stable subordinator.

Data source	\hat{A} estimated using \hat{H} from Table 2		Joint estimates \hat{A} and \hat{H}	
	\hat{H}	\hat{A}	\hat{H}	\hat{A}
Well 1 $s_n < 10$	0.86	0.06 (0.05; 0.07)	0.87 (0.78; 0.97)	0.05 (0.02; 0.13)
Well 1 $s_n > 12$	0.10	2.12 (1.84; 2.45)	0.14 (0.10; 0.20)	2.00 (1.66; 2.43)
Well 2 $s_n < 10$	0.87	0.12 (0.11; 0.13)	0.91 (0.86; 0.96)	0.08 (0.04; 0.16)
Well 2 $s_n > 12$	0.08	5.14 (4.48; 5.90)	0.10 (0.06; 0.16)	5.27 (4.56; 6.08)
Well 3 $s_n < 10$	0.85	0.16 (0.14; 0.17)	0.89 (0.82; 0.96)	0.11 (0.05; 0.23)
Well 3 $s_n > 12$	0.11	4.02 (3.60; 4.49)	0.09 (0.06; 0.14)	4.02 (3.59; 4.51)
Well 4 $s_n < 10$	0.70	0.21 (0.19; 0.24)	0.76 (0.70; 0.83)	0.16 (0.11; 0.23)
Well 4 $s_n > 12$	0.11	1.80 (1.67; 1.94)	0.13 (0.11; 0.16)	1.74 (1.59; 1.90)
Well 5 $s_n < 10$	0.66	0.18 (0.15; 0.23)	0.70 (0.53; 0.93)	0.15 (0.06; 0.37)
Well 5 $s_n > 12$	0.16	1.36 (1.13; 1.65)	0.25 (0.22; 0.30)	0.84 (0.64; 1.11)
Well 6 $s_n < 10$	0.75	0.09 (0.08; 0.11)	0.81 (0.70; 0.94)	0.06 (0.03; 0.14)
Well 6 $s_n > 12$	0.17	0.86 (0.78; 0.94)	0.18 (0.15; 0.22)	0.80 (0.66; 0.96)

788
789
790

791 Table 4. Estimates \hat{C} of C given estimates \hat{H} of H from Table 2, and joint estimates \hat{C}
792 and \hat{H} , of PVs with associated 95% confidence limits (in parenthesis) for all wells at $s_n < 10$ and
793 $s_n > 12$ in the case of lognormal subordinator.

Data source	\hat{C} estimated using \hat{H} from Table 2		Joint estimates \hat{C} and \hat{H}	
	\hat{H}	\hat{C}	\hat{H}	\hat{C}
Well 1 $s_n < 10$	0.86	0.52 (0.46; 0.58)	0.85 (0.75; 0.96)	0.53 (0.40; 0.70)
Well 1 $s_n > 12$	0.10	13.22 (12.36; 14.13)	0.07 (0.05; 0.08)	17.877 (15.44; 20.70)
Well 2 $s_n < 10$	0.87	1.35 (1.18; 1.53)	0.84 (0.74; 0.96)	1.43 (1.07; 1.92)
Well 2 $s_n > 12$	0.08	39.31 (36.17; 42.72)	0.04 (0.03; 0.07)	55.61 (45.31; 68.24)
Well 3 $s_n < 10$	0.85	0.87 (0.76; 1.00)	0.83 (0.72; 0.95)	0.91 (0.67; 1.25)
Well 3 $s_n > 12$	0.11	19.96 (18.30; 21.77)	0.09 (0.06; 0.12)	24.88 (18.72; 33.06)
Well 4 $s_n < 10$	0.70	1.09 (0.92; 1.31)	0.65 (0.52; 0.80)	1.23 (0.85; 1.80)
Well 4 $s_n > 12$	0.11	10.02 (9.48; 10.59)	0.08 (0.07; 0.09)	13.01 (11.66; 14.52)
Well 5 $s_n < 10$	0.66	1.59 (1.35; 1.88)	0.61 (0.50; 0.75)	1.78 (1.25; 2.53)
Well 5 $s_n > 12$	0.16	8.69 (7.73; 9.76)	0.09 (0.08; 0.11)	16.05 (13.83; 18.61)
Well 6 $s_n < 10$	0.76	2.52 (2.15; 2.95)	0.71 (0.60; 0.84)	2.77 (1.98; 3.89)
Well 6 $s_n > 12$	0.17	26.90 (24.45; 29.58)	0.14 (0.11; 0.17)	37.02 (27.90; 49.11)

794
795
796

797 Table 5. POT sample sizes and Kolmogorov-Smirnov p -values associated with three lags in
 798 various wells.

s_n	Well No.	No. of samples	No. of POT samples	p -value (KS test)
1	1	3566	177	0.240
	2	4048	202	0.994
	3	2944	147	0.706
	4	3881	194	0.437
	5	6948	208	0.970
	6	4265	213	0.788
32	1	3535	177	0.612
	2	4017	201	0.199
	3	2913	146	0.394
	4	3850	191	0.426
	5	6917	208	0.313
	6	4203	210	0.215
1024	1	2543	126	0.089
	2	3025	151	0.530
	3	1921	96	0.928
	4	2858	143	0.473
	5	5925	178	0.072
	6	2219	111	0.590

799
 800 Table 6. Method of moments estimates of H for POTs at $s_n < 10$ (denoted by subscript w) and s_n
 801 > 12 (subscript b).

Well	\hat{H}_w	\hat{H}_b
1 (Maroon field)	0.84	0.02
2 (Maroon field)	0.83	0.0001
3 (Maroon field)	0.80	0.06
4 (Ahwaz field)	0.61	0.03
5 (Ahwaz field)	0.60	0.02
6 (Tabnak field)	0.71	0.11

803
 804
 805

806

Figure Captions

807 Figure 1: Variation of neutron porosity (P) with depth in Wells 1 (Maroon field), 4 - 5 (Ahwaz
808 field) and 6 (Tabnak field).

809 Figure 2. Frequency distributions on arithmetic and semi-logarithmic scales of $P' = P - P_a$ in
810 (a)-(b) Well 1 (Maroon field), (c)-(d) Well 4 (Ahwaz field), and (e)-(f) Well 6 (Tabnak
811 field). Also shown are ML fits of Gaussian (dashed), α -stable (solid red), and NLN
812 (black solid) pdfs.

813 Figure 3. Increments $\Delta P(s_n)$ of P at normalized lags $s_n = 1$ ($s = 0.15$ m), 32 ($s = 4.80$ m), and
814 1024 ($s = 153.60$ m) versus sequential (integer) vertical position in (a) - (c) Well 1
815 (Maroon field), (d) - (f) Well 4 (Ahwaz field), and (g) - (i) Well 6 (Tabnak field).

816 Figure 4. Frequency distributions of increments $\Delta P(s_n)$ of P at normalized lags $s_n = 1$ ($s = 0.15$
817 m), 32 ($s = 4.80$ m), and 1024 ($s = 153.60$ m) in (a) - (c) Well 1 (Maroon field) and (d) -
818 (f) Well 4 (Ahwaz field). Also shown are ML fits of Gaussian (dashed), α -stable (solid
819 red), and NLN (black solid) pdfs.

820 Figure 5. Frequency distributions of increments $\Delta P(s_n)$ of P at normalized lags $s_n = 1$ ($s = 0.15$
821 m) and 1024 ($s = 153.60$ m) in Well 6 (Tabnak field). Also shown are ML fits of
822 Gaussian (dashed), α -stable (solid red), and NLN (black solid) pdfs.

823 Figure 6. ML estimates $\hat{\alpha}$ and $\hat{\sigma}$ of stability and scale parameters, respectively, characterizing
824 α -stable distribution models of increments $\Delta P(s_n)$ of P in all wells versus normalized
825 lag.

826 Figure 7. $S_N^q(s_n)$ versus normalized lag for $q = 0.5, 1.0,$ and 2.0 in Wells 1 (Maroon) and 6
827 (Tabnak). Red dashed line demarcates breaks in power-law scaling regimes. Logarithmic

828 scale regression lines and corresponding power-law relations between $S_N^q(s_n)$ and s_n are
 829 given in (a) for Well 1 at $s_n < 10$, (b) Well 1 at $s_n > 12$, (c) Well 6 at $s_n < 10$, and (d) Well
 830 6 at $s_n > 12$.

831 Figure 8. S_N^{q+1} versus S_N^q for $q = 1, 2$ and 3 in Wells 1 (Maroon) and 6 (Tabnak). Logarithmic
 832 scale regression lines and corresponding power-law relations between S_N^{q+1} versus S_N^q are
 833 given in (a) for Well 1 at $s_n < 10$, (b) Well 1 at $s_n > 12$, (c) Well 6 at $s_n < 10$, and (d) Well
 834 6 at $s_n > 12$.

835 Figure 9. $\zeta_w(q)$ and $\zeta_b(q)$ evaluated as functions of q by the method of moments (M) and ESS in
 836 (a) Well 1 at $s_n < 10$, (b) Well 1 at $s_n > 12$, (c) Well 6 at $s_n < 10$, and (d) Well 6 at $s_n > 12$.

837 Figure 10. Sample scale parameter square $\hat{\sigma}^2(s_n)$ as functions of s_n (squares), ML fitted PVs
 838 (solid lines) and 95% confidence limits (broken curves) in Wells 1 and 6 based on (a) -
 839 (b) estimates \hat{A} given estimates \hat{H} from Table 2 and (c) - (d) joint estimates of \hat{A} and
 840 \hat{H} .

841 Figure 11. Sample structure functions, $S_N^2(s_n)$, of order $q = 2$ as functions of s_n (squares), ML
 842 fitted PVs (solid lines) and 95% confidence limits (broken curves) in Wells 1 and 6 based
 843 on (a) - (b) estimates \hat{C} given estimates \hat{H} from Table 2 and (c) - (d) joint estimates of
 844 \hat{C} and \hat{H} .

845 Figure 12. POTs of absolute increments $|\Delta P(s_n)|$ at normalized lags $s_n = 1, 32$, and 1024 versus
 846 sequential (integer) vertical position in (a) - (c) Well 1 (Maroon), (d) - (f) Well 4
 847 (Ahwaz), and (g) - (i) Well 6 (Tabnak).

848 Figure 13. Quantile-quantile plots of GPD fits to frequency distributions of POTs of *porosity*
 849 increments at normalized lag $s_n = 1, 32$ and 1024 in (a)-(c) Well 1 (Maroon), (d)-(f) Well

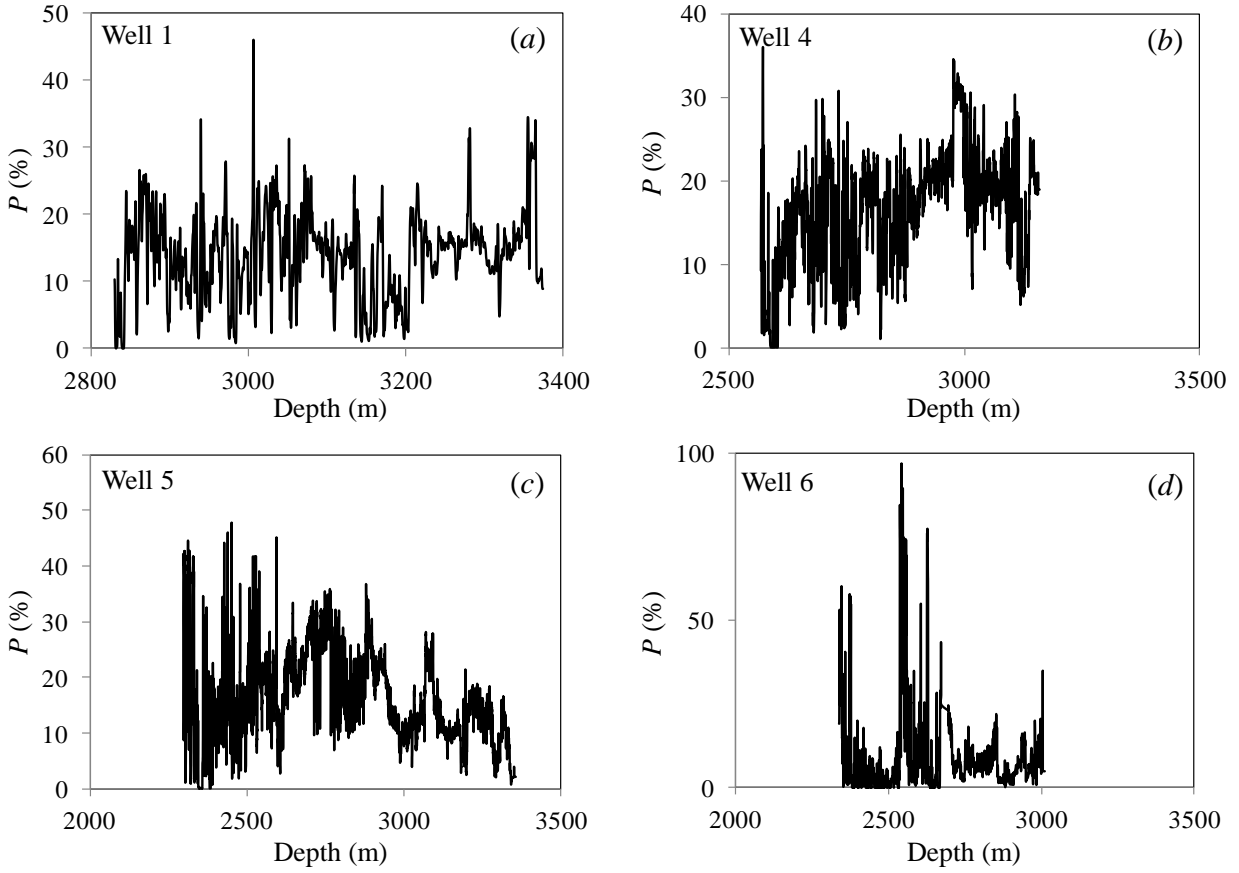
850 4 (Ahwaz), and (g)-(i) Well 6 (Tabnak). Also shown are a line of unit slope (solid), 95%
851 confidence intervals (dashed), and p -values of Kolmogorov-Smirnov tests.

852 Figure 14. Variations of best fit GPD shape (ζ_{POT}) and scale (σ_{POT}) parameters with normalized
853 lag in (a) - (b) Well 1 (Maroon), (c) - (d) Well 4 (Ahwaz), and (e)-(f) Well 6 (Tabnak).
854 Also shown are 95% uncertainty bounds.

855 Figure 15. $S_{N_{POT}}^q(s_n)$ versus normalized lag for $q = 0.5, 1.0, \text{ and } 2.0$ in Wells 1 (Maroon) and 6
856 (Tabnak). Red dashed line demarcates breaks in power-law scaling regimes. Logarithmic
857 scale regression lines and corresponding power-law relations between $S_{N_{POT}}^q(s_n)$ and s_n
858 are given in (a) for Well 1 at $s_n < 10$, (b) Well 1 at $s_n > 12$, (c) Well 6 at $s_n < 10$, and (d)
859 Well 6 at $s_n > 12$.

860 Figure 16. $\zeta_w(q)$ and $\zeta_b(q)$ evaluated for POTs as functions of q by the method of moments (M)
861 and ESS in (a) Well 1 at $s_n < 10$, (b) Well 1 at $s_n > 12$, (c) Well 6 at $s_n < 10$, and (d) Well
862 6 at $s_n > 12$.

863



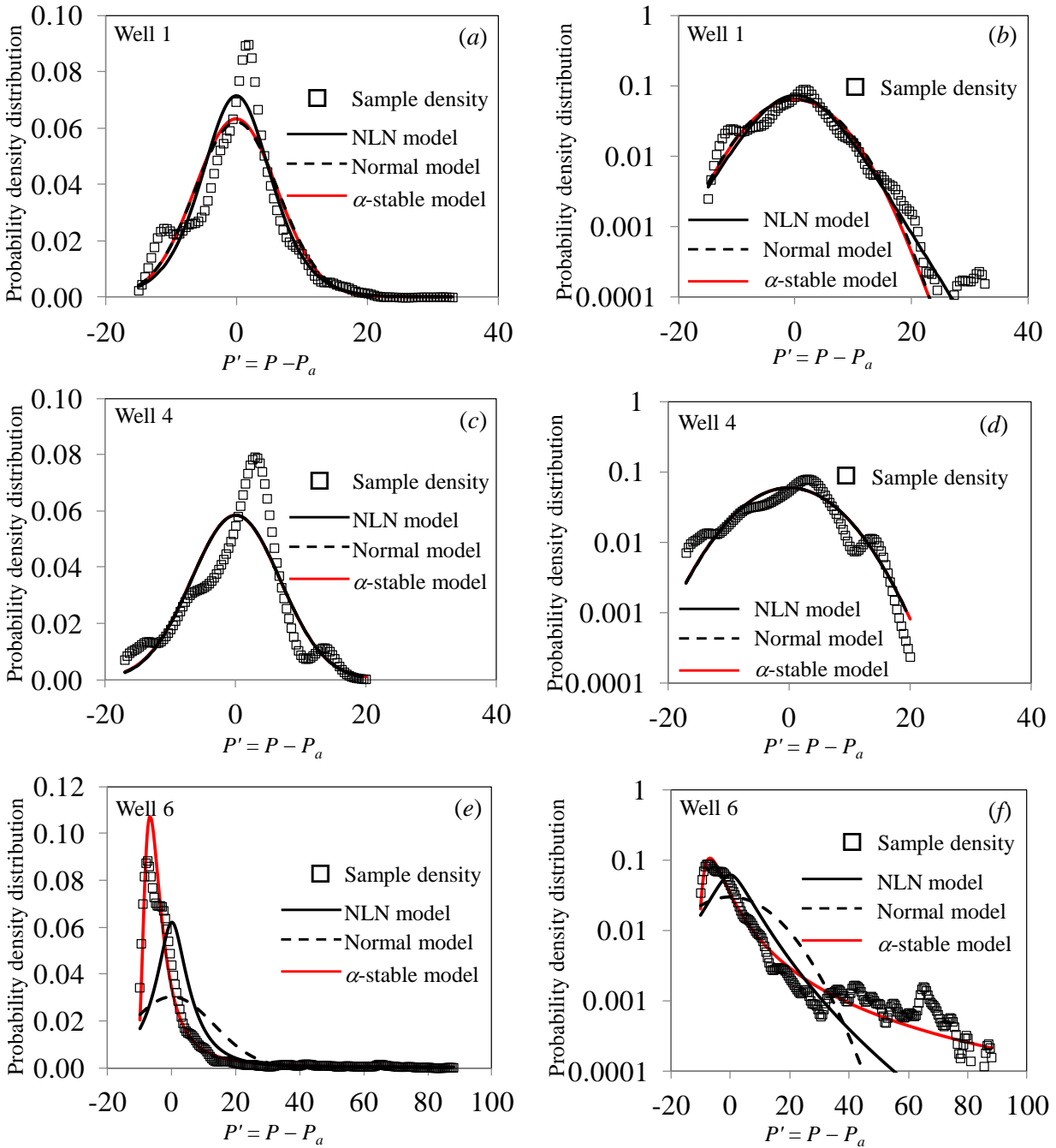
864

865 Figure 1: Variation of neutron porosity (P) with depth in Wells 1 (Maroon field), 4 - 5 (Ahwaz

866

field) and 6 (Tabnak field).

867



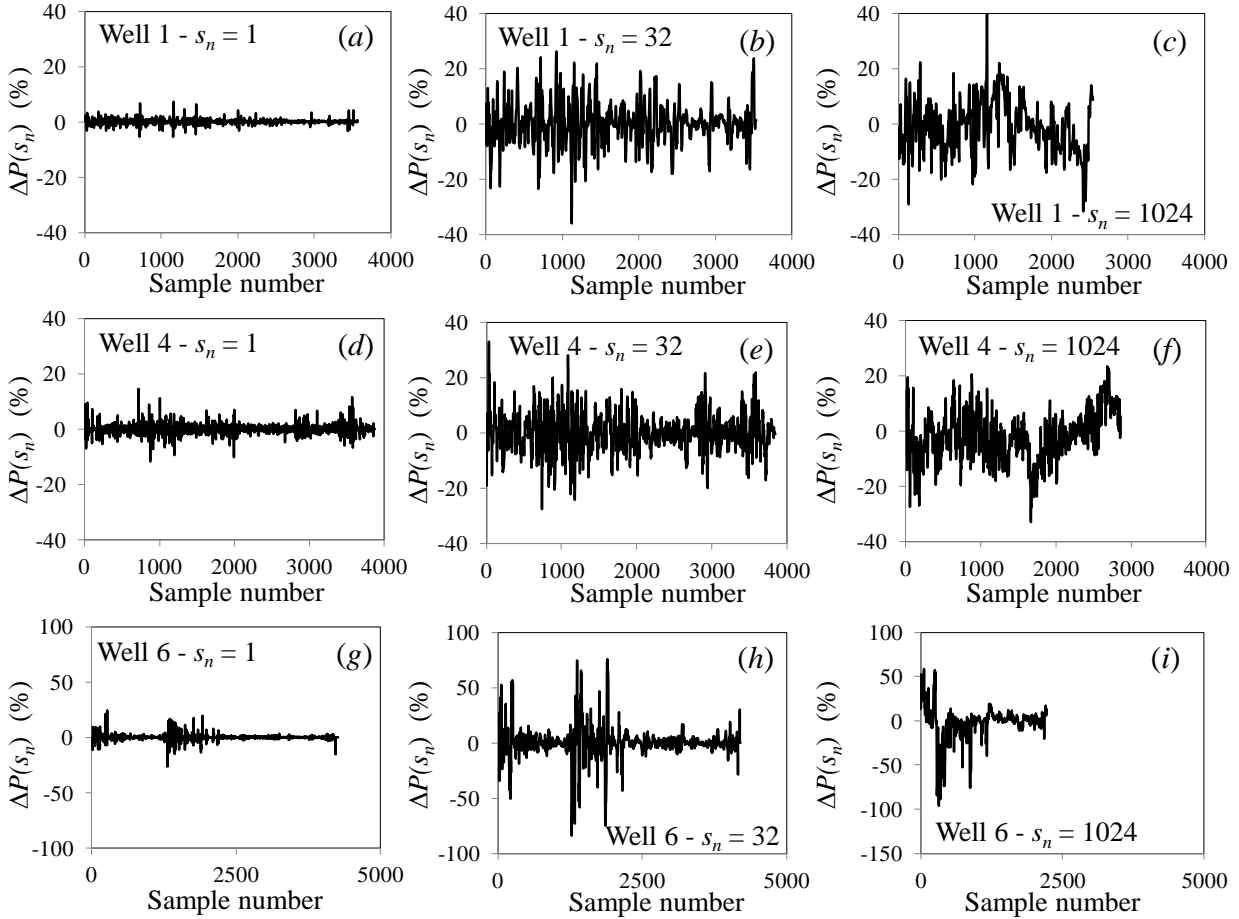
868

869 Figure 2. Frequency distributions on arithmetic and semi-logarithmic scales of $P' = P - P_a$ in

870 (a)-(b) Well 1 (Maroon field), (c)-(d) Well 4 (Ahwaz field), and (e)-(f) Well 6 (Tabnak field).

871 Also shown are ML fits of Gaussian (dashed), α -stable (solid red), and NLN (black solid) pdfs.

872



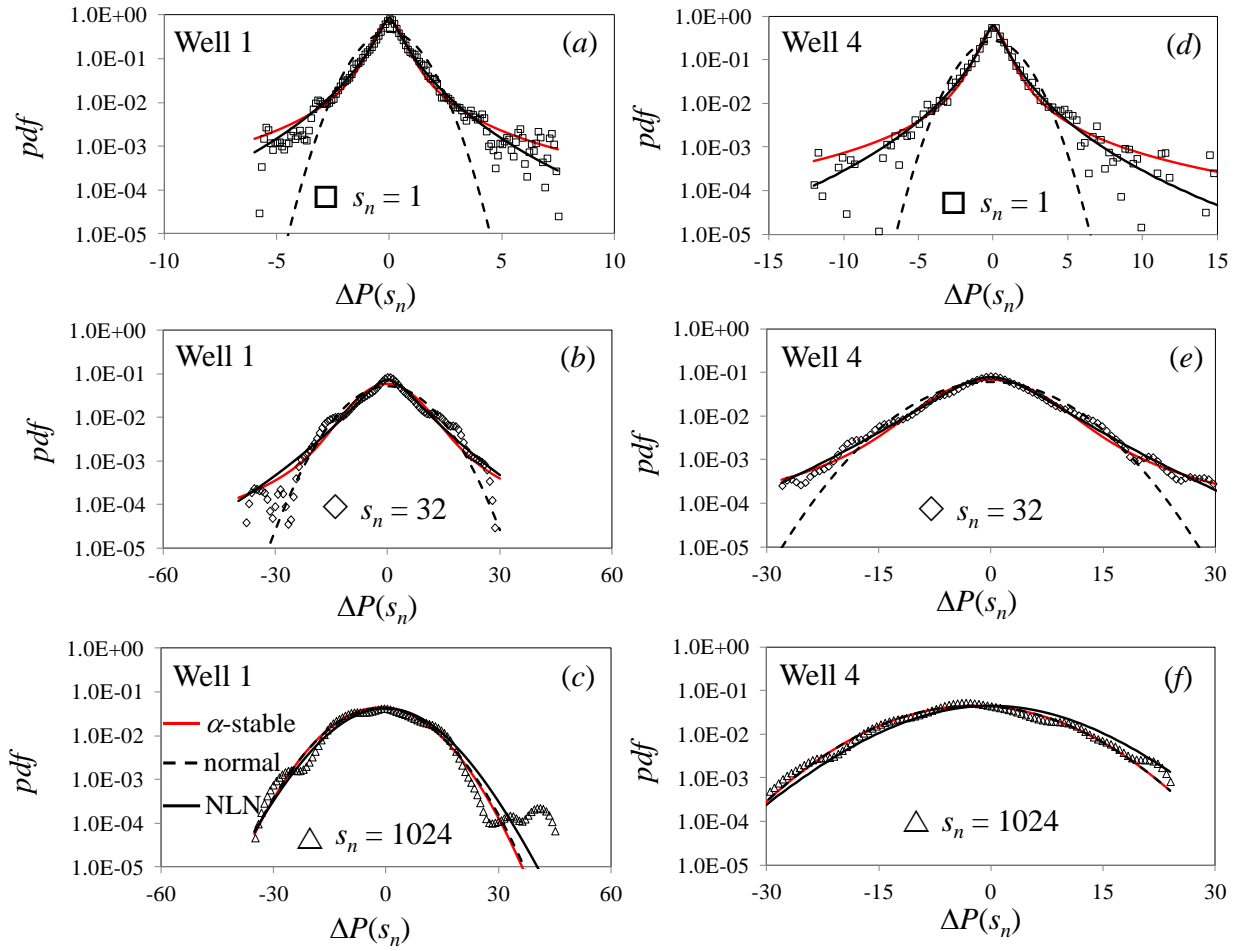
873

874 Figure 3. Increments $\Delta P(s_n)$ of P at normalized lags $s_n = 1$ ($s = 0.15$ m), 32 ($s = 4.80$ m), and

875 1024 ($s = 153.60$ m) versus sequential (integer) vertical position in (a) - (c) Well 1 (Maroon

876 field), (d) - (f) Well 4 (Ahwaz field), and (g) - (i) Well 6 (Tabnak field).

877

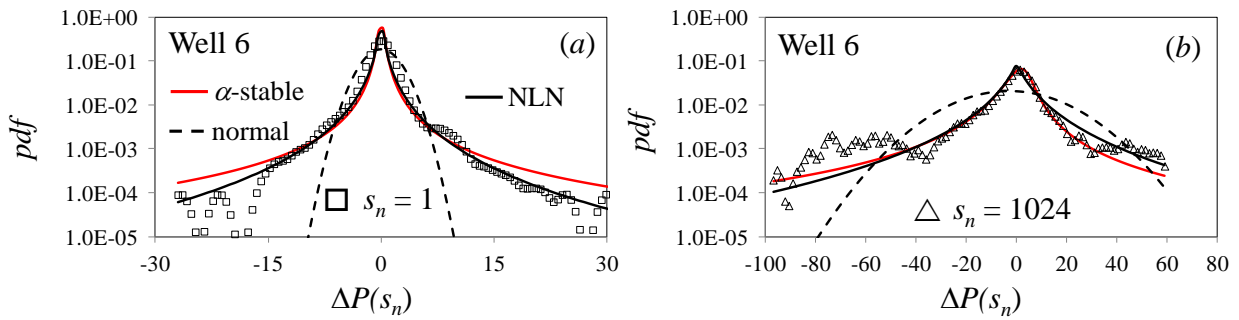


878

879 Figure 4. Frequency distributions of increments $\Delta P(s_n)$ of P at normalized lags $s_n = 1$ ($s = 0.15$
 880 m), 32 ($s = 4.80$ m), and 1024 ($s = 153.60$ m) in (a) - (c) Well 1 (Maroon field) and (d) - (f) Well
 881 4 (Ahwaz field). Also shown are ML fits of Gaussian (dashed), α -stable (solid red), and NLN
 882 (black solid) pdfs.

883

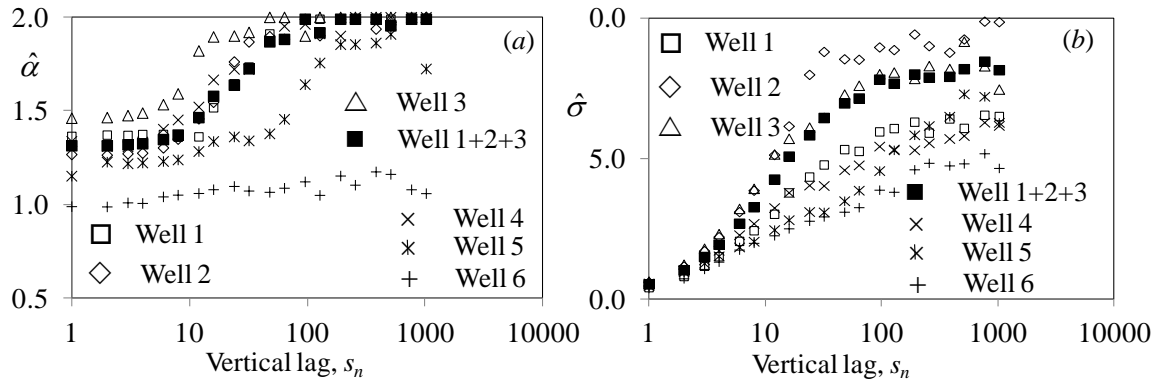
884
885
886
887



888
889
890
891
892
893

Figure 5. Frequency distributions of increments $\Delta P(s_n)$ of P at normalized lags $s_n = 1$ ($s = 0.15$ m) and 1024 ($s = 153.60$ m) in Well 6 (Tabnak field). Also shown are ML fits of Gaussian (dashed), α -stable (solid red), and NLN (black solid) pdfs.

894

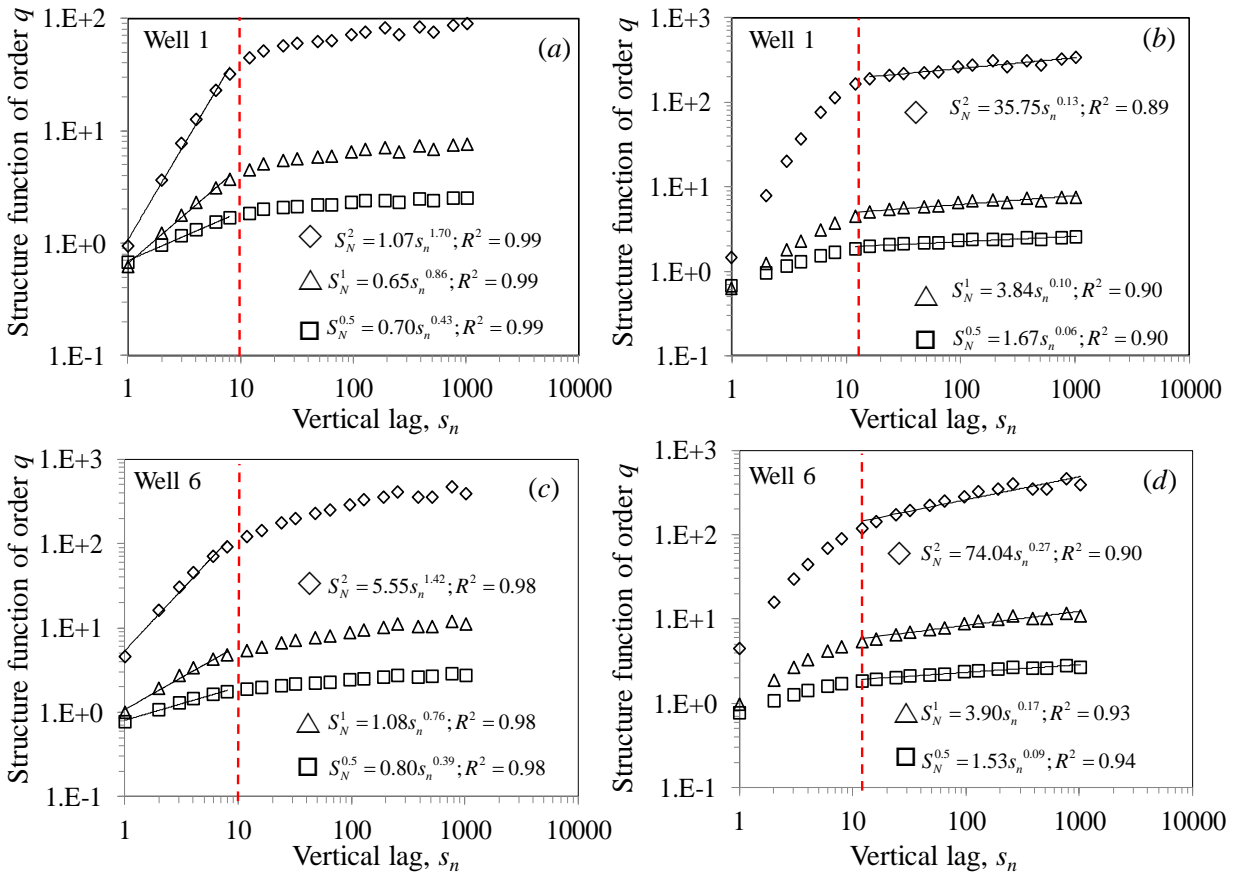


895

896 Figure 6. ML estimates $\hat{\alpha}$ and $\hat{\sigma}$ of stability and scale parameters, respectively, characterizing

897 α -stable distribution models of increments $\Delta P(s_n)$ of P in all wells versus normalized lag.

898



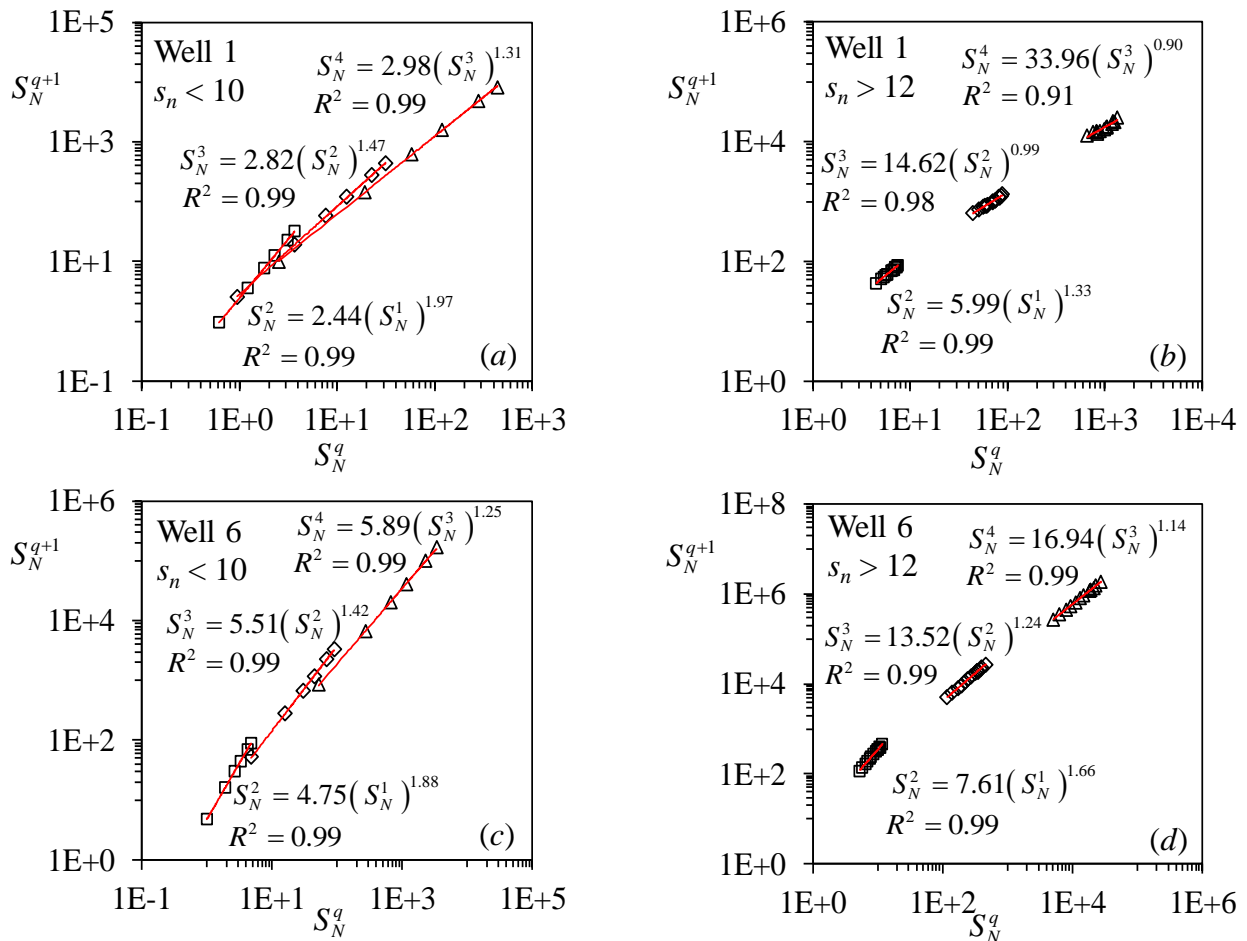
900

901 Figure 7. $S_N^q(s_n)$ versus normalized lag for $q = 0.5, 1.0,$ and 2.0 in Wells 1 (Maroon) and 6
 902 (Tabnak). Red dashed line demarcates breaks in power-law scaling regimes. Logarithmic scale

903 regression lines and corresponding power-law relations between $S_N^q(s_n)$ and s_n are given in (a)

904 for Well 1 at $s_n < 10,$ (b) Well 1 at $s_n > 12,$ (c) Well 6 at $s_n < 10,$ and (d) Well 6 at $s_n > 12.$

905



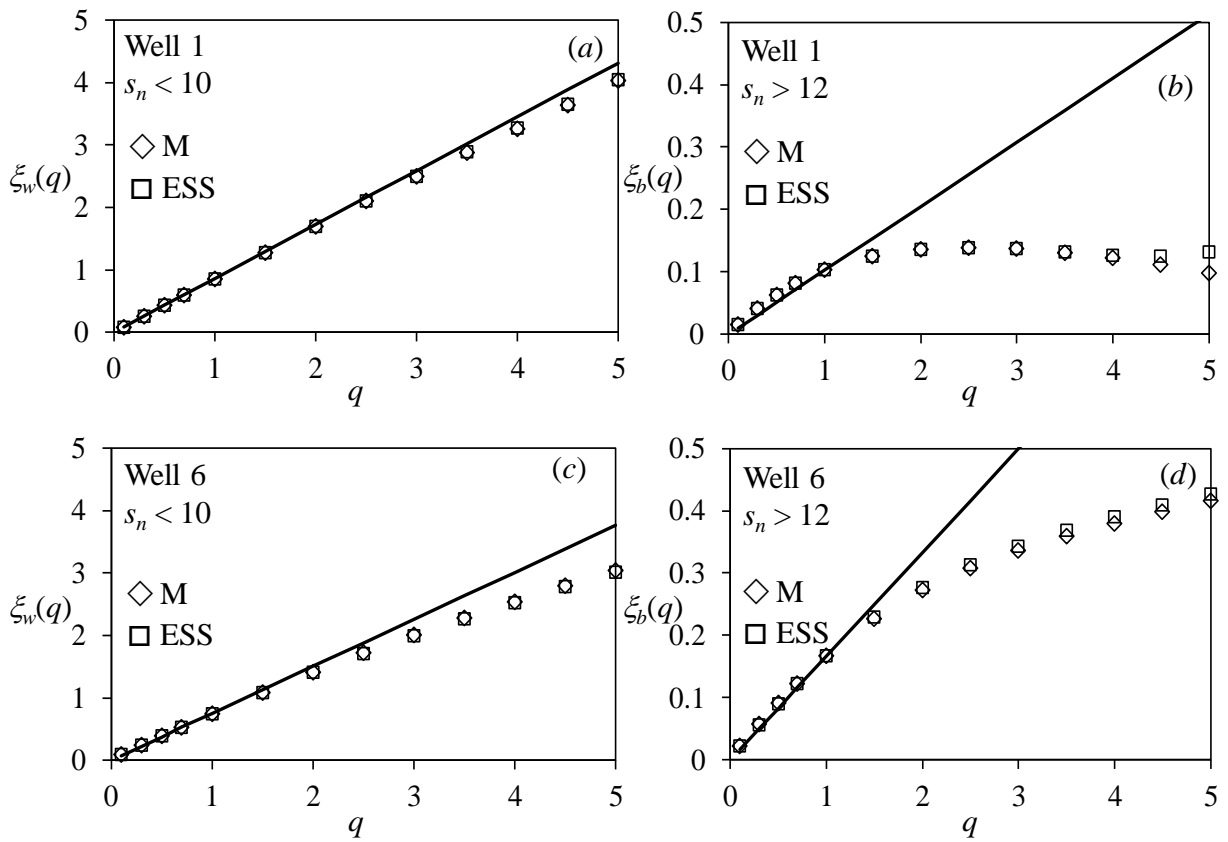
907

908 Figure 8. S_N^{q+1} versus S_N^q for $q = 1, 2$ and 3 in Wells 1 (Maroon) and 6 (Tabnak). Logarithmic

909 scale regression lines and corresponding power-law relations between S_N^{q+1} versus S_N^q are given

910 in (a) for Well 1 at $s_n < 10$, (b) Well 1 at $s_n > 12$, (c) Well 6 at $s_n < 10$, and (d) Well 6 at $s_n > 12$.

911

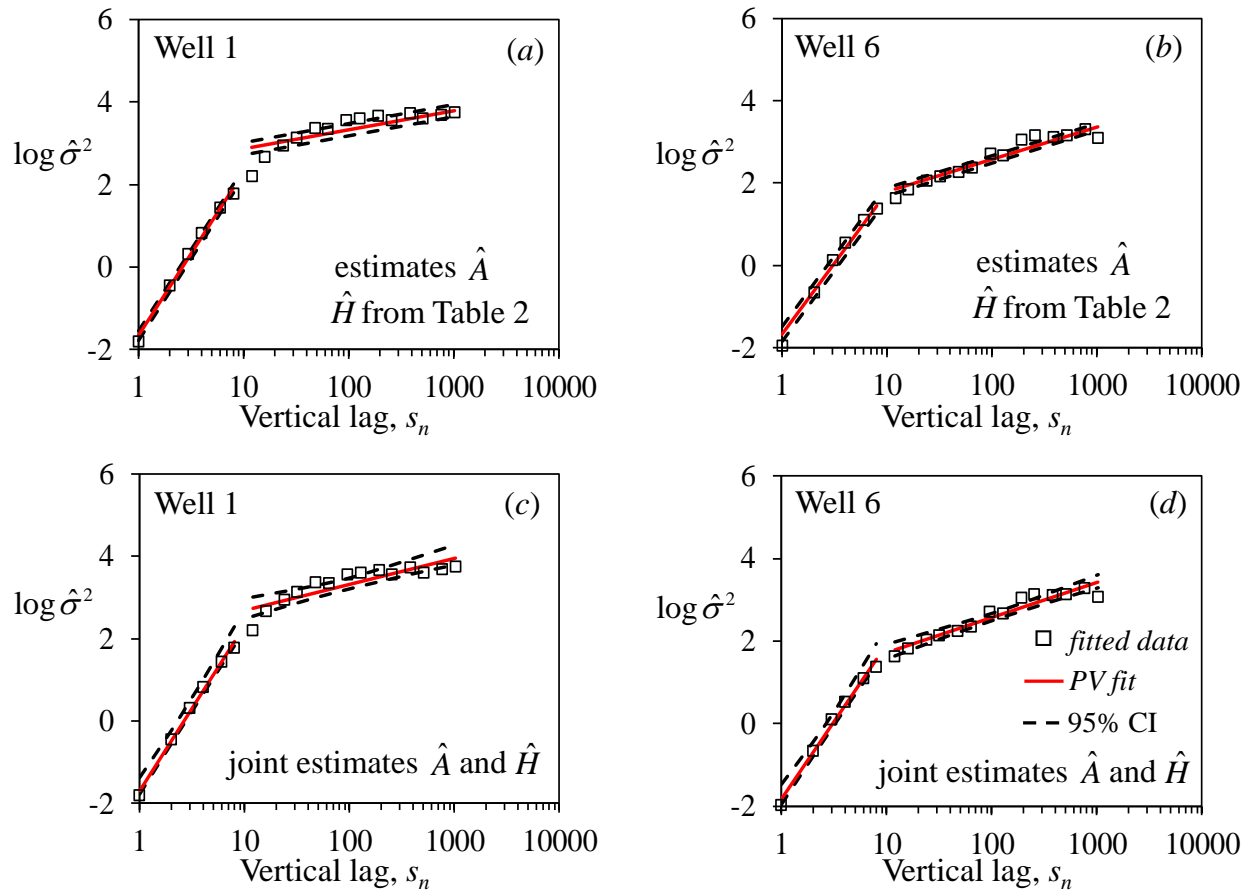


913

914 Figure 9. $\xi_w(q)$ and $\xi_b(q)$ evaluated as functions of q by the method of moments (M) and ESS in

915 (a) Well 1 at $s_n < 10$, (b) Well 1 at $s_n > 12$, (c) Well 6 at $s_n < 10$, and (d) Well 6 at $s_n > 12$.

916



918

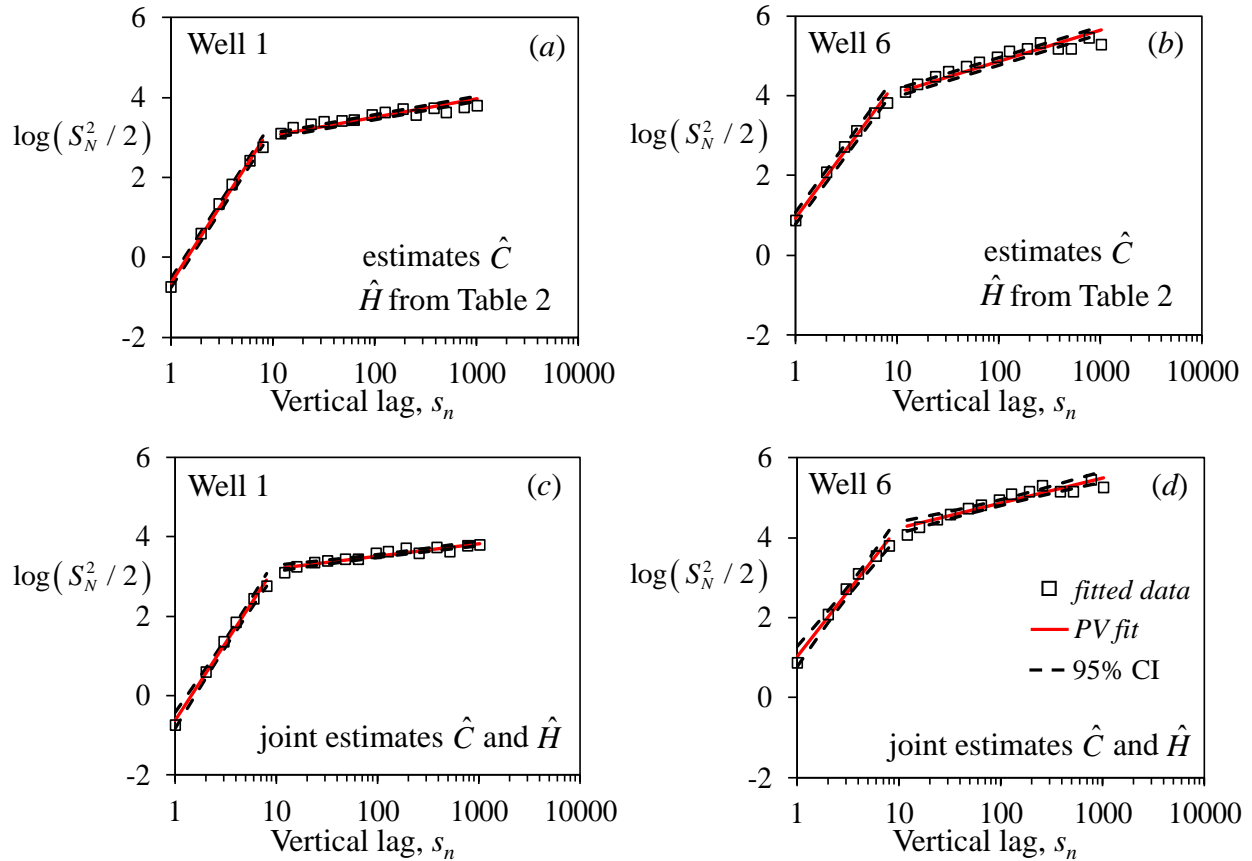
919 Figure 10. Sample scale parameters $\hat{\sigma}^2(s_n)$ as functions of s_n (squares), ML fitted PVs (solid

920 lines) and 95% confidence limits (broken curves) in Wells 1 and 6 based on (a) - (b) estimates

921 \hat{A} given estimates \hat{H} from Table 2 and (c) - (d) joint estimates of \hat{A} and \hat{H} .

922

923



924

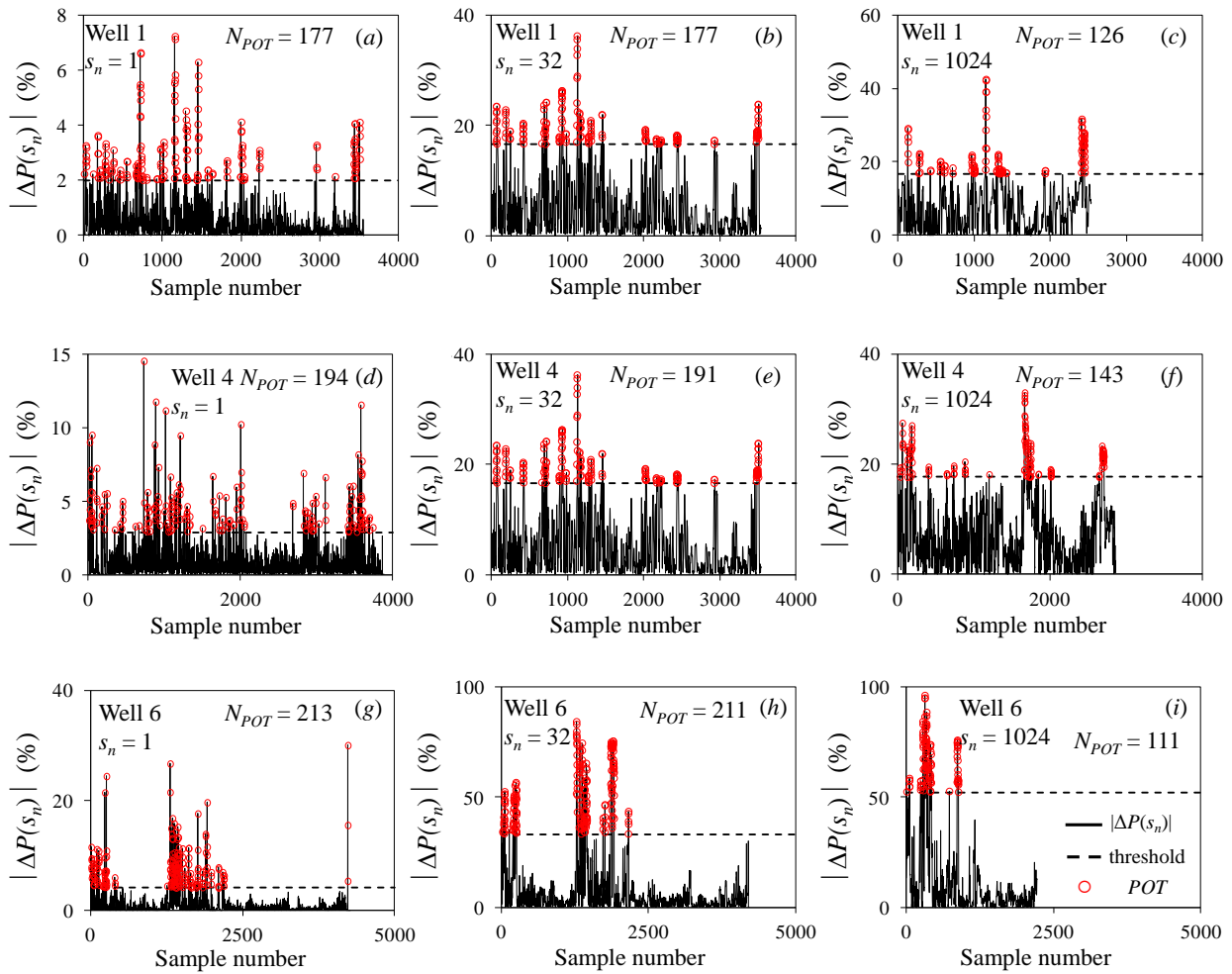
925 Figure 11. Sample structure functions, $S_N^2(s_n)$, of order $q = 2$ as functions of s_n (squares), ML

926 fitted PVs (solid lines) and 95% confidence limits (broken curves) in Wells 1 and 6 based on (a)

927 - (b) estimates \hat{C} given estimates \hat{H} from Table 2 and (c) - (d) joint estimates of \hat{C} and \hat{H} .

928

929



931

932 Figure 12. POTs of absolute increments $|\Delta P(s_n)|$ at normalized lags $s_n = 1, 32,$ and 1024 versus

933 sequential (integer) vertical position in (a) - (c) Well 1 (Maroon), (d) - (f) Well 4 (Ahwaz), and

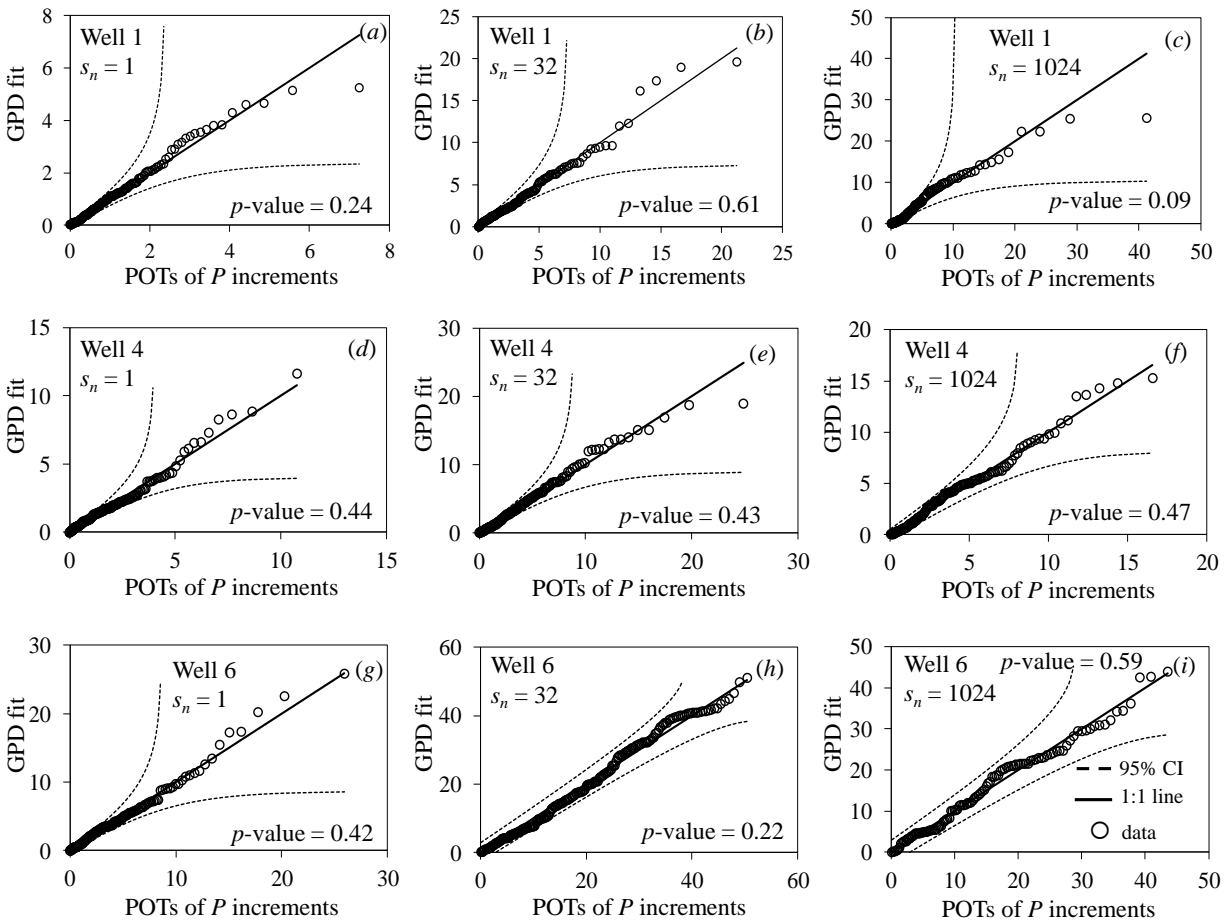
934

(g) - (i) Well 6 (Tabnak).

935

936

937



938

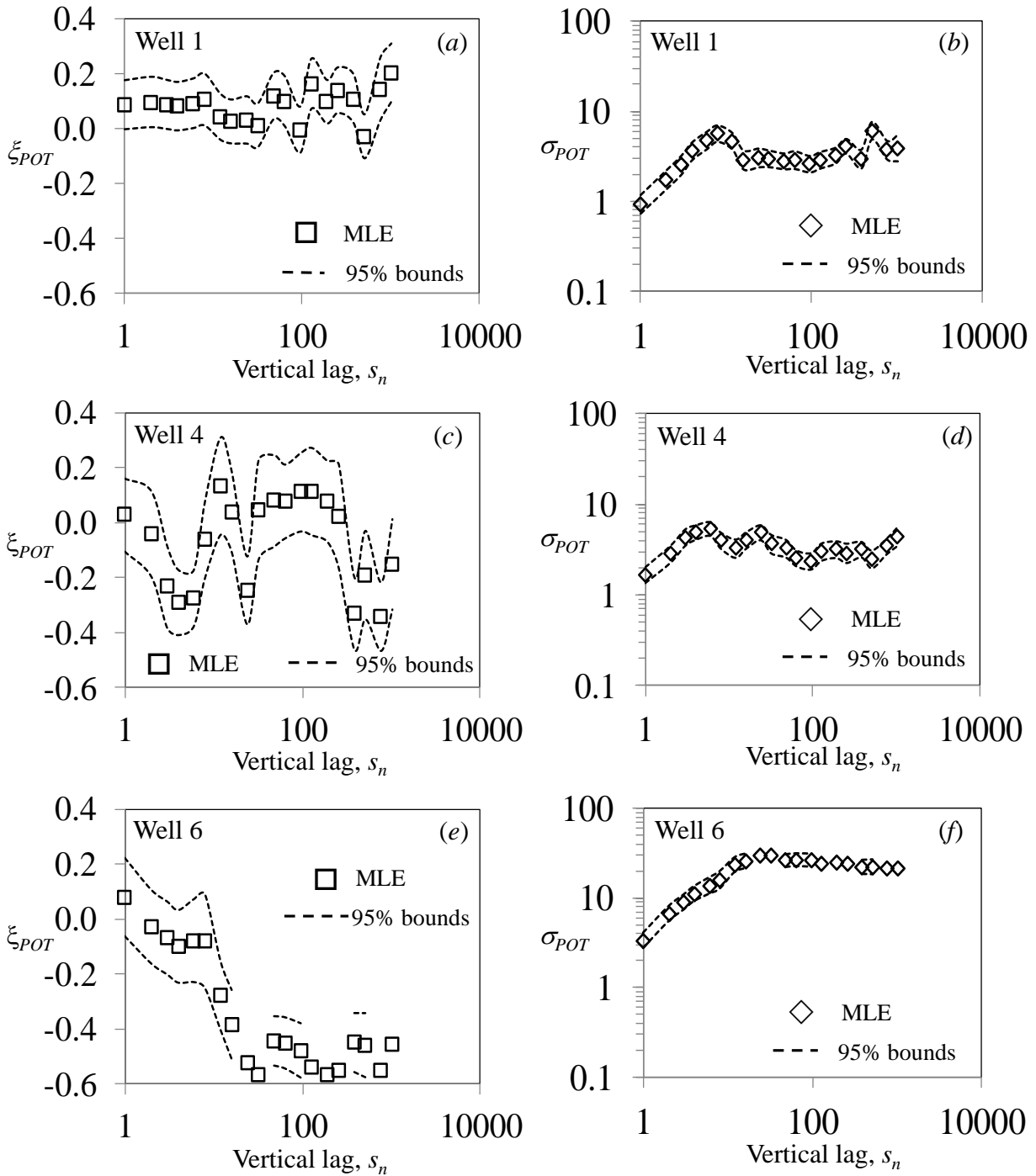
939 Figure 13. Quantile-quantile plots of GPD fits to frequency distributions of POTs of P

940 increments at normalized lag $s_n = 1, 32$ and 1024 in (a)-(c) Well 1 (Maroon), (d)-(f) Well 4

941 (Ahwaz), and (g)-(i) Well 6 (Tabnak). Also shown are a line of unit slope (solid), 95%

942 confidence intervals (dashed), and p -values of Kolmogorov-Smirnov tests.

943



944

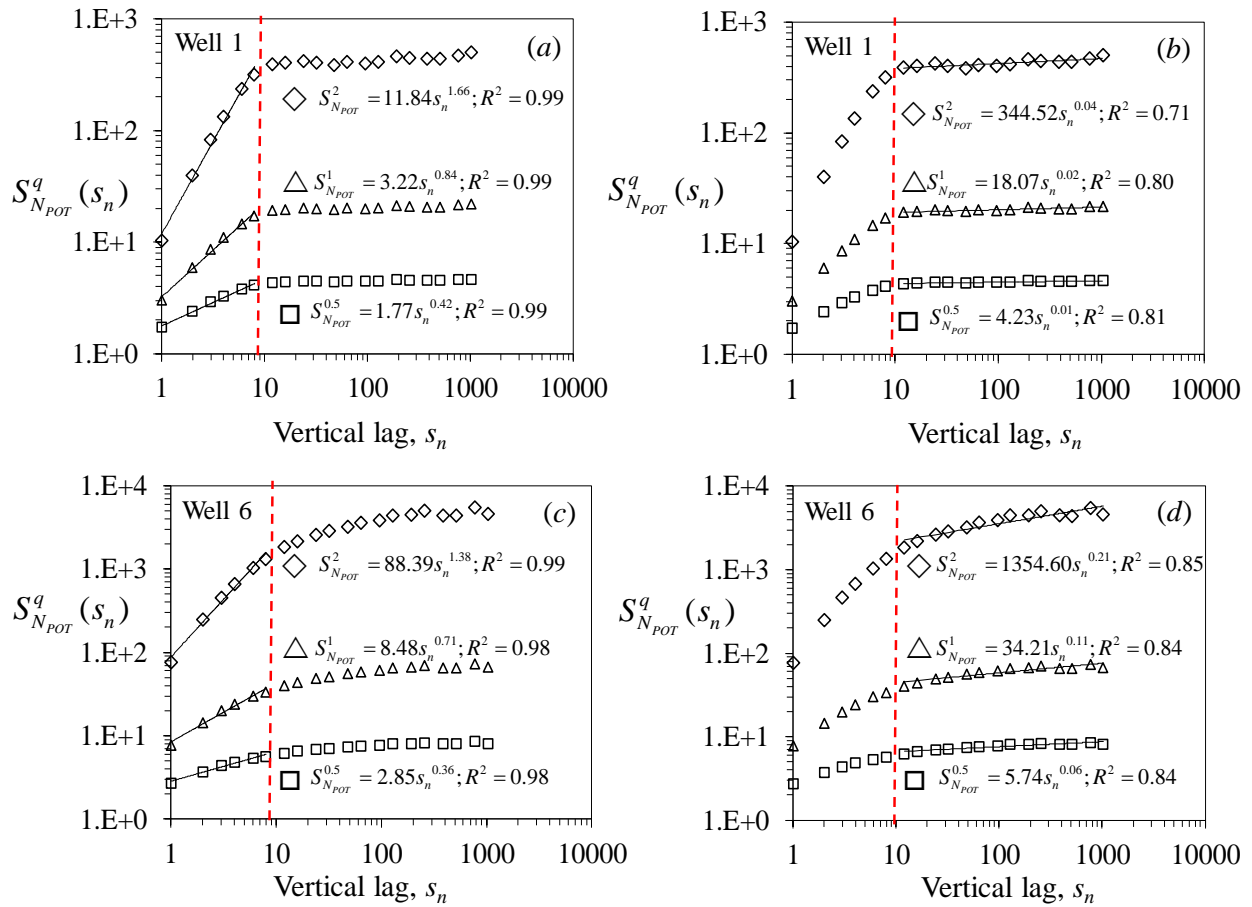
945 Figure 14. Variations of best fit GPD shape (ξ_{POT}) and scale (σ_{POT}) parameters with normalized

946 lag in (a) - (b) Well 1 (Maroon), (c) - (d) Well 4 (Ahwaz), and (e)-(f) Well 6 (Tabnak). Also

947

shown are 95% uncertainty bounds.

948



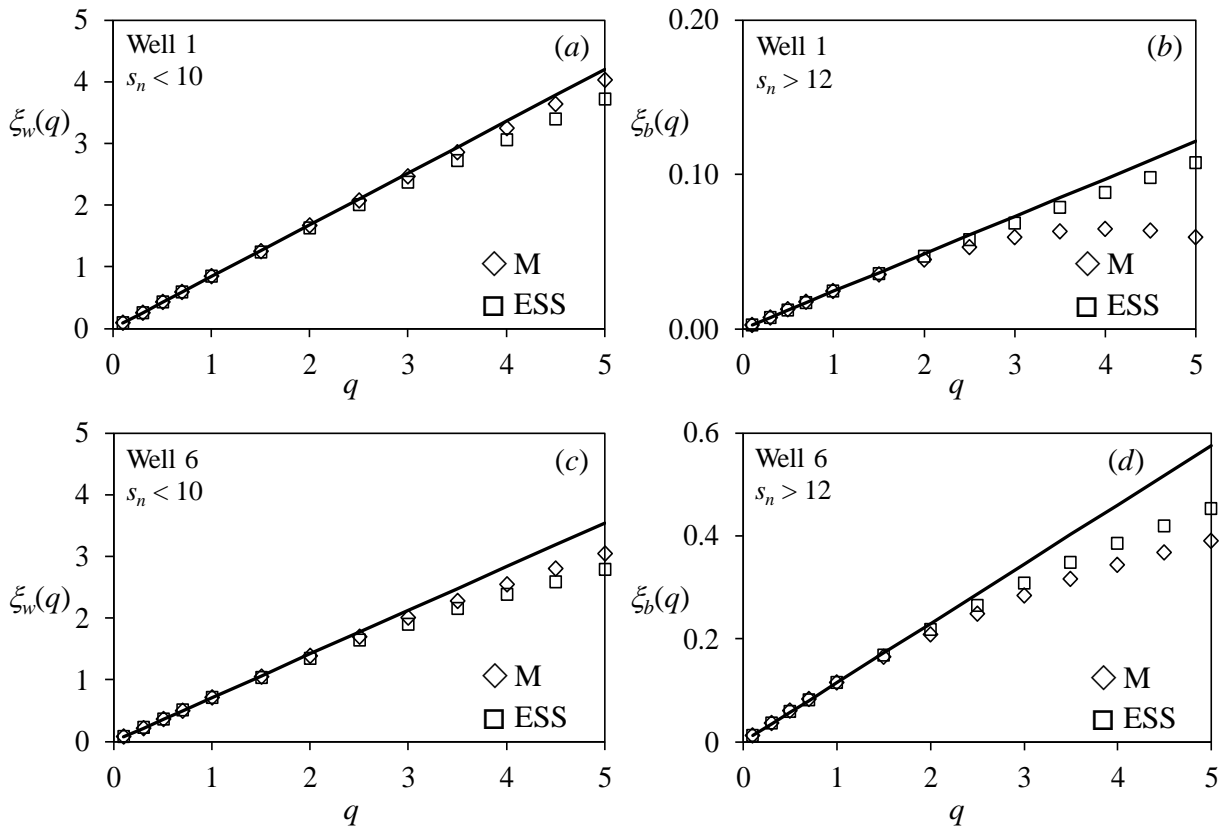
950

951 Figure 15. $S_{N_{POT}}^q(s_n)$ versus normalized lag for $q = 0.5, 1.0,$ and 2.0 in Wells 1 (Maroon) and 6
 952 (Tabnak). Red dashed line demarcates breaks in power-law scaling regimes. Logarithmic scale
 953 regression lines and corresponding power-law relations between $S_{N_{POT}}^q(s_n)$ and s_n are given in
 954 (a) for Well 1 at $s_n < 10$, (b) Well 1 at $s_n > 12$, (c) Well 6 at $s_n < 10$, and (d) Well 6 at $s_n > 12$.

955

956

957



959

960 Figure 16. $\xi_w(q)$ and $\xi_b(q)$ evaluated for POTs as functions of q by the method of moments (M)

961 and ESS in (a) Well 1 at $s_n < 10$, (b) Well 1 at $s_n > 12$, (c) Well 6 at $s_n < 10$, and (d) Well 6 at s_n

962

> 12.

963